Fluid Phase Equilibria 504 (2020) 112306

Contents lists available at ScienceDirect

Fluid Phase Equilibria

journal homepage: www.elsevier.com/locate/fluid

Guide to efficient solution of PC-SAFT classical Density Functional Theory in various Coordinate Systems using fast Fourier and similar Transforms

Rolf Stierle*, Elmar Sauer, Johannes Eller, Marc Theiss, Philipp Rehner, Philipp Ackermann, Joachim Gross*

Institute of Thermodynamics and Thermal Process Engineering, University of Stuttgart, Pfaffenwaldring 9, 70569, Stuttgart, Germany

ARTICLE INFO

Article history:
Received 21 June 2019
Received in revised form
12 August 2019
Accepted 1 September 2019
Available online 25 September 2019

Keywords:
Density functional theory
PC-SAFT
Fast fourier transform
Fast hankel transform
Fast sine transform
Fast cosine transform

ABSTRACT

Classical density functional theory (DFT) is a powerful tool for studying solvation or problems where resolution of interfacial domains or interfacial properties among phases (or thin films) is required. Many interesting problems necessitate multi-dimensional modeling, which calls for robust and efficient algorithmic implementations of the Helmholtz energy functionals. A possible approach for achieving efficient numerical solutions is using the convolution theorem of the Fourier transform. This study is meant to facilitate research and application of DFT methods, by providing a detailed guide on solving DFT problems in multi-dimensional domains. Methods for efficiently solving the convolution integrals in Fourier space are presented for Cartesian, cylindrical, and spherical coordinates. For cylindrical and spherical coordinate systems, rotational and spherical symmetry is exploited, respectively. To enable easy implementation, our approach is based on fast Fourier, fast Hankel, fast sine and cosine transforms on equidistant grids, all of which can be applied using off-the-shelf algorithms. Subtle details for implementing algorithms in cylindrical and spherical coordinate systems are emphasized. The work covers functionals based on weighted densities exemplarily. Functionals according to fundamental measure theory (FMT) as well as a Helmholtz energy functional based on the perturbed-chain statistical associating fluid theory (PC-SAFT) equation of state are worked out in detail (and given as Supporting Information).

1. Introduction

Efficient numerical solution of convolution integrals is important for solving classical density functional theory (DFT) or dynamic density functional theory (DDFT) in multidimensional problems. The solution of a DFT model, namely the densities of all species, is obtained iteratively. The computational demand for the iterative solution is the repetitive computation of numerous convolution integrals. Naïve numerical convolution through integration leads to long computation times and complicated integration schemes, especially for multidimensional DFT problems. One approach to address this problem is the utilization of the convolution theorem of the Fourier transform. The $\mathcal{O}(N \log N)$ computational complexity of fast Fourier transform (FFT) algorithms (compared to $\mathcal{O}(N^2)$ for numerical convolution) leads to a significant advantage regarding computational performance. Additionally, working with integral transforms like FFT simplifies multidimensional convolutions, because each dimension can be treated separately which averts multidimensional integration schemes.

Several authors applied integral transforms to convolution integrals appearing in DFT. Knepley et al. [1] used the FFT approach for convolutions in a DFT for ionic solutions. A short introduction to usage of FFT for Rosenfeld's fundamental measure theory [2] (FMT) was also given. Frink et al. [3,4] proposed Fourier space convolution on a multidimensional Cartesian grid in combination with nonlinear iterative solvers and Sears and Frink [5] proposed using FFT in combination with a matrix-free scheme and compared computational efficiency for one-, two- and three-dimensional systems. Hlushak et al. [6] employed the FFT on a two-dimensional Cartesian grid to analyze flexible chain molecules at

* Corresponding authors.
E-mail addresses: stierle@itt.uni-stuttgart.de (R. Stierle), gross@itt.uni-stuttgart.de (J. Gross).

https://doi.org/10.1016/j.fluid.2019.112306
0378-3812/

curved surfaces, whereas Hlushak et al. [7,8] studied attractive particles in nanopores. While analyzing rotationally symmetric systems, rotational symmetry was not exploited in the computation of the convolution integrals, leading to unnecessary computational overhead. Oettel et al. applied the Fourier convolution approach within the framework of three-dimensional FMT and compared results to those obtained by phase-field models [10] and Monte Carlo simulations [9]. A similar analysis of crystal structures and solid-liquid interfaces using three-dimensional FMT combined with a Helmholtz energy contribution to account for attractive interactions was conducted by Wang et al. [11]. Solvation effects in water were studied by Levesque et al. [12]; solvation energies of amino acid side chains by Liu et al. [13], both by three-dimensional DFT. Zhou et al. [14] applied three-dimensional Cartesian DFT to heterogeneous nucleation of Lennard-Jones fluids on solid walls.

For cylindrical systems, rotational symmetry can be exploited to reduce dimensionality of the DFT problem. In one-dimensional cylindrical coordinates, González et al. [15] proposed using the Hankel transform for computation of the convolution in Fourier space. The fast Hankel transform was not employed, however. Malijevský [16] and Mariani et al. [17] took advantage of rotational symmetry to formulate the convolution integrals of FMT for cylindrical coordinates in real space. In Fourier space this was done by Boţan et al. [18] for the analysis of hard-sphere fluids in annular wedges. In cylindrical coordinates the Fourier transform can not be computed using FFT, but requires a, preferably fast, Hankel transform algorithm for the radial direction. Boţan et al. [18] reformulated the DFT problem on a logarithmic grid to apply a fast Hankel transform.

Spherical symmetry can be exploited to efficiently compute spherical DFT systems in one dimension. This was applied by González et al. [15] to hard spheres in a spherical cavity, utilizing Fourier space convolution. For FMT in spherical coordinates projection of the weight functions onto one dimension was described by Roth [19].

Convolution in Fourier space by exploiting the FFT or similar algorithms is not the only approach to speed up the computation of the convolution integrals appearing in DFT problems. Yatsyshin et al. introduced a Chebyshev pseudo-spectral collocation method in combination with Clenshaw-Curtis quadrature for computation of the convolution integrals in one [20] and two dimensions [21] of a Cartesian grid, extended by Nold et al. [22]. Contrary to FFT convolution, equidistant grid spacing is not required, but possible. Problem-specific grid spacing has potential to reduce computational effort. Xu and Cao [23] used a two-dimensional multiscale finite element approach to reduce computational complexity for the convolution integrals.

Computation time, of course, not only depends on the performance of the Helmholtz functional computation and the involved convolution integrals but also depends on the algorithm used to solve the system of nonlinear equations as well. Previous work on numerical algorithms can be found in Kovalenko et al. [24], Frink and Salinger [25,26], Frink et al. [3,4], Frink et al. [27], a comparison of different nonlinear solvers in Mairhofer and Gross [28].

Classical DFT or DDFT are theoretical approaches that carry molecular detail through averaged quantities. DFT approaches are predictive when a suitable Helmholtz energy functional is applied. We aim at applying FFT convolution to a functional consistent with the perturbed-chain statistical associating fluid theory (PC-SAFT) equation of state [29,30]. The PC-SAFT equation of state is formulated in terms of the Helmholtz energy allowing easy generalization to Helmholtz energy functionals. PC-SAFT provides good descriptions of thermodynamic properties in bulk phases for a wide variety of real substances and mixtures, including components of low molecular mass [30], but also complex species like polymers [31] or associating substances [32]. The underlying molecular model regards molecules as hard chains with attractive van der Waals segment-segment interactions or hydrogen-bonding (associating) [32–37] or dipolar and quadrupolar interactions [38–40]. Several approaches combining PC-SAFT and DFT have been proposed. Gross [41] described a DFT for pure substances which was generalized by Klink and Gross for mixtures and successfully applied to vapor-liquid [42], liquid-liquid interfaces [43]. Klink et al. [44] and Lamanna et al. [45] applied this PC-SAFT DFT to interfacial transport resistivities. Sauer and Gross [46] suggested a Helmholtz energy functional for the dispersion contribution based on a weighted density approximation suitable for confined systems, predicting physical phenomena like surface tension, contact angles [47] and adsorption isotherms. Similar approaches were taken by Shen et al. [48,49], Ye et al. [50] and Xu et al. [51].

This work provides a practical guide to implementing and solving DFT models that are based on weighted densities. We wish to facilitate the use of DFT approaches in engineering applications. More specifically we demonstrate implementation of the ideal gas, hard-sphere, hard-chain and dispersion contribution of PC-SAFT DFT in Cartesian, cylindrical and spherical coordinate systems. We use the FFT algorithm for Cartesian coordinates and the axial contribution to cylindrical systems, the fast Hankel transform is applied for the radial contribution to cylindrical systems and the fast sine and cosine transform is adopted for systems described in spherical coordinates. In contrast to previous work using cylindrical coordinates [18], we apply the fast Hankel transform of Hansen [52,53], which allows computation of Hankel transforms on equidistant (rather than logarithmic) grids by using a combination of fast Abel [54] and fast sine and cosine transforms. Equidistant grids reduce computational overhead because a smaller number of overall grid points is usually possible, while maintaining the same worst-case grid density as compared to logarithmic grids. Fourier space convolution is easier to implement than naïve real space convolution, which allows writing robust simulation codes.

The general procedure is shown for weighted density approximations in the main part of this work. A detailed description of equations for Helmholtz energy functionals based on the PC-SAFT equation of state is provided in the Supporting Information, including functional derivatives of the model as well as a comprehensive introduction to Fourier space convolution.

2. Classical density functional theory

The starting point for classical DFT is the grand potential functional Ω, which, for a mixture of N_c components is written as

$$\Omega[\{\rho_i(\mathbf{r})\}] = F[\{\rho_i(\mathbf{r})\}] + \sum_{i=1}^{N_c} \int \rho_i(\mathbf{r}) \left(V_i^{\text{ext}}(\mathbf{r}) - \mu_i\right) \mathrm{d}\mathbf{r} \tag{1}$$

with Helmholtz energy functional F, chemical potential μ_i of component i and the external potential V_i^{ext}, acting on component i. Although not made explicit in this notation, the specified variables of Ω are temperature T, volume V, and chemical potentials μ_i of all species. Square brackets denote a functional dependence and curly brackets around $\{\rho_i(\mathbf{r})\}$ indicate a vector of all densities within a mixture, $i = 1, \cdots, N_c$.

In equilibrium the grand potential functional is minimal and the value of the grand potential functional reduces to the grand potential $\Omega^0 = \Omega[\{\rho_i^0\}]$. The minimum implies, that for the equilibrium density profile $\{\rho_i^0(\mathbf{r})\}$, the functional derivatives of the grand potential functional Ω with respect to the density profiles $\{\rho_i(\mathbf{r})\}$ vanish, according to

$$\left.\frac{\delta\Omega[\{\rho_i\}]}{\delta\rho_j(\mathbf{r})}\right|_{\{\rho_i^0(\mathbf{r})\}} = 0 \tag{2}$$

which leads to the main equation of DFT

$$\frac{\delta F[\{\rho_i\}]}{\delta\rho_j(\mathbf{r})} = \mu_j - V_j^{\text{ext}}(\mathbf{r}) \qquad \forall j \tag{3}$$

that can be solved for the density profiles $\{\rho_i^0(\mathbf{r})\}$ in the considered volume, provided a model for the Helmholtz energy functional is available.

2.1. Weighted density approximation functionals

Weighted density approximation functionals can be constructed generically as

$$\beta F[\{\rho_i(\mathbf{r})\}] = \int \Phi(\{n_\alpha(\mathbf{r}), \mathbf{n}_\beta(\mathbf{r})\})\, \mathrm{d}\mathbf{r} \tag{4}$$

where $\alpha \in \{1, \cdots\}$ is a generic index that denotes the scalar-valued weighted densities and $\beta \in \{\mathrm{V1}, \cdots\}$ points at the vector-valued weighted densities, with $\beta F = \frac{F}{k_\mathrm{B}T}$, where k_B is the Boltzmann constant, and with the reduced Helmholtz energy density Φ, which is solely a function of the weighted densities $n_{\alpha,\beta}$. The weighted densities $n_{\alpha,\beta}$ are calculated via convolution of the density profile $\{\rho_i\}$ as

$$n_{\alpha,\beta}(\mathbf{r}) = \sum_{i=1}^{N_\mathrm{c}} \int \rho_i(\mathbf{r}')\omega_i^{\alpha,\beta}(\mathbf{r}-\mathbf{r}')\, \mathrm{d}\mathbf{r}' \equiv \sum_{i=1}^{N_\mathrm{c}} \rho_i(\mathbf{r}) \otimes \omega_i^{\alpha,\beta}(\mathbf{r}) \tag{5}$$

the respective weight functions ω_i^α are typically defined as functions including Heaviside step functions Θ, Dirac delta functions δ, or derivatives thereof δ' as shown for scalar-valued weight functions

$$\omega_i^\alpha(\mathbf{r}) \propto \Theta(R_i - |\mathbf{r}|) \tag{6a}$$

$$\omega_i^\alpha(\mathbf{r}) \propto \delta(R_i - |\mathbf{r}|) \tag{6b}$$

$$\omega_i^\alpha(\mathbf{r}) \propto \delta'(R_i - |\mathbf{r}|) \tag{6c}$$

Vector-valued weight functions are expressed as combinations of the previous weights with the position vector $\mathbf{r}$ as

$$\omega_i^\beta(\mathbf{r}) \propto \frac{\mathbf{r}}{|\mathbf{r}|}\omega_i^\alpha(\mathbf{r}) \tag{7}$$

For the case of eq. (6a) one averages over a spherical volume, whereas for the case of eq. (6b), the weighting is defined on the surface of a sphere with radius R_i. The functional derivative is calculated as

$$\begin{aligned} \frac{\delta\beta F^{\text{hs}}[\{\rho_i\}]}{\delta\rho_j(\mathbf{r})} &= \int \frac{\delta\Phi}{\delta\rho_j(\mathbf{r})}\, \mathrm{d}\mathbf{r}' \\ &= \int \sum_{\alpha,\beta} \frac{\partial\Phi}{\partial n_{\alpha,\beta}(\mathbf{r}')} \frac{\delta n_{\alpha,\beta}(\mathbf{r}')}{\delta\rho_j(\mathbf{r})}\, \mathrm{d}\mathbf{r}' \end{aligned} \tag{8}$$

with the functional derivative of the weighted densities, according to

$$\begin{aligned} \frac{\delta n_{\alpha,\beta}(\mathbf{r}')}{\delta\rho_j(\mathbf{r})} &= \frac{\delta}{\delta\rho_j(\mathbf{r})} \sum_{i=1}^{N_\mathrm{c}} \int \rho_i(\mathbf{r}'')\omega_i^{\alpha,\beta}(\mathbf{r}'-\mathbf{r}'')\, \mathrm{d}\mathbf{r}'' \\ &= \sum_{i=1}^{N_\mathrm{c}} \int \delta_{ij}\delta(\mathbf{r}''-\mathbf{r})\omega_i^{\alpha,\beta}(\mathbf{r}'-\mathbf{r}'')\, \mathrm{d}\mathbf{r}'' \\ &= \omega_j^{\alpha,\beta}(\mathbf{r}'-\mathbf{r}) \end{aligned} \tag{9}$$

with δ_{ij} as the Kronecker delta and δ as the Dirac delta function. Substitution of eq. (9) in eq. (8) allows the functional derivative to be rewritten as a sum of convolution integrals, according to

$$\begin{aligned} \frac{\delta\beta F^{\text{hs}}[\{\rho_i\}]}{\delta\rho_j(\mathbf{r})} &= \sum_{\alpha,\beta} \int \frac{\partial\Phi}{\partial n_{\alpha,\beta}} \omega_j^{\alpha,\beta}(\mathbf{r}'-\mathbf{r})\, \mathrm{d}\mathbf{r}' \\ &= \sum_\alpha \frac{\partial\Phi}{\partial n_\alpha} \otimes \omega_j^\alpha - \sum_\beta \frac{\partial\Phi}{\partial \mathbf{n}_\beta} \otimes \omega_j^\beta \end{aligned} \tag{10}$$

The scalar-valued weight functions are even, with

$$\omega_i^\alpha(\mathbf{r}'-\mathbf{r}) = \omega_i^\alpha(\mathbf{r}-\mathbf{r}') \qquad \text{for } \alpha \in \{1, \cdots\} \tag{11}$$

while the vector-valued weight functions are odd functions

$$\boldsymbol{\omega}_i^\beta(\mathbf{r}'-\mathbf{r}) = -\boldsymbol{\omega}_i^\beta(\mathbf{r}-\mathbf{r}') \qquad \text{for } \beta \in \{\mathrm{V1}, \cdots\} \tag{12}$$

leading to the minus signs in eq. (10).

3. Fourier space convolutions

Weighted density approximation functionals and functional derivatives can be calculated efficiently in Fourier space, by making use of the convolution theorem of the Fourier transform. In this section we show how to compute the required Fourier transforms in various coordinate systems using off-the-shelf FFT, fast Hankel, fast sine/cosine transform algorithms.

We show the procedure by considering weighted densities as convolutions of density ρ_i with weight function ω_i. One transforms the density profile ρ_i to Fourier space using a discrete transform scheme and, after multiplication in Fourier space with the analytically transformed weight function, transforms the result back to real space using the inverse discrete transform scheme, according to

$$\begin{aligned} n_{\alpha,\beta}(\mathbf{r}) &= \int \rho_i(\mathbf{r}')\omega_i^{\alpha,\beta}(\mathbf{r}-\mathbf{r}')\, \mathrm{d}\mathbf{r}' = \rho_i(\mathbf{r}) \otimes \omega_i^{\alpha,\beta}(\mathbf{r}) \\ &= \mathscr{F}^{-1}\left[\mathscr{F}[\rho_i(\mathbf{r})]\mathscr{F}\left[\omega_i^{\alpha,\beta}(\mathbf{r})\right]\right] \\ &= \mathscr{F}^{-1}\left[\widehat{\rho}_i(\mathbf{k})\widehat{\omega}_i^{\alpha,\beta}(\mathbf{k})\right] \end{aligned} \tag{13}$$

with the Fourier space vector $\mathbf{k}$, and introducing the Fourier transform $\mathscr{F}$ and inverse Fourier transform operator $\mathscr{F}^{-1}$. The circumflex $\widehat{\ }$ above quantities indicates them being the Fourier transforms of the respective quantity.

The scalar-valued weight functions in Fourier space, eq. (6), are obtained using

$$\widehat{\omega}_i^\alpha(\mathbf{k}) = \mathscr{F}\left[\omega_i^\alpha(\mathbf{r})\right] \tag{14}$$

The vector-valued weight functions in Fourier space can be described by

$$\widehat{\omega}_i^{\beta}(\mathbf{k}) \propto -\mathrm{i}\,\mathbf{k}\widehat{\omega}_i^{\alpha}(\mathbf{k}) \tag{15}$$

where the position vector $\frac{\mathbf{r}}{|\mathbf{r}|}$ in eq. (7) transforms to $(-\mathrm{i}\,\mathbf{k})$ in Fourier space, with the imaginary unit i.

3.1. Convolution in cartesian coordinates

For Cartesian coordinates we substitute $\mathbf{r} = [x, y, z]^{\top}$ and $\mathbf{k} = [k_x, k_y, k_z]^{\top}$. The Fourier transform of the density profiles is computed as

$$\widehat{\rho}_i(k_x, k_y, k_z) = \mathscr{F}_x \mathscr{F}_y \mathscr{F}_z[\rho_i(x, y, z)] \tag{16}$$

just as presented in Appendix A in eq. (A.6). For computation of the scalar-valued weighted densities

$$n_{\alpha}(x, y, z) = \sum_{i=1}^{N_c} \mathscr{F}_x^{-1} \mathscr{F}_y^{-1} \mathscr{F}_z^{-1}\left[\widehat{\rho}_i(k_x, k_y, k_z)\widehat{\omega}_i^{\alpha}(k_x, k_y, k_z)\right] \tag{17}$$

the inverse Fourier transform for scalar functions, eq. (A.7), is needed. For the vector-valued weighted densities we use the vector-valued weight functions in Fourier space from eq. (15). The inverse Fourier transform is obtained as

$$\mathbf{n}_{\beta}(x, y, z) = \sum_{i=1}^{N_c} \mathscr{F}^{-1}\left[-\mathrm{i}\,\mathbf{k}\widehat{\omega}_i^{\alpha}(\mathbf{k})\widehat{\rho}_i(\mathbf{k})\right] \tag{18}$$

with

$$\begin{aligned} &\mathscr{F}^{-1}\left[-\mathrm{i}\,\mathbf{k}\widehat{\omega}_i^{\alpha}(\mathbf{k})\widehat{\rho}_i(\mathbf{k})\right] \\ &= \begin{pmatrix} \mathscr{F}_x^{-1}\mathscr{F}_y^{-1}\mathscr{F}_z^{-1}\left[-\mathrm{i}\;k_x\;\widehat{\omega}_i^{\alpha}(k_x, k_y, k_z)\widehat{\rho}_i(k_x, k_y, k_z)\right] \\ \mathscr{F}_x^{-1}\mathscr{F}_y^{-1}\mathscr{F}_z^{-1}\left[-\mathrm{i}\;k_y\;\widehat{\omega}_i^{\alpha}(k_x, k_y, k_z)\widehat{\rho}_i(k_x, k_y, k_z)\right] \\ \mathscr{F}_x^{-1}\mathscr{F}_y^{-1}\mathscr{F}_z^{-1}\left[-\mathrm{i}\;k_z\;\widehat{\omega}_i^{\alpha}(k_x, k_y, k_z)\widehat{\rho}_i(k_x, k_y, k_z)\right] \end{pmatrix} \end{aligned} \tag{19}$$

using the inverse Fourier transform for vector-valued functions from eq. (A.14). The convolution integrals of the Helmholtz energy density derivatives $\frac{\partial\Phi}{\partial n_{\alpha}}$ with the weight functions ω_i^{α} are computed similarly.

The scalar-valued convolution integrals in eq. (10) are obtained using the scalar inverse Fourier transform from eq. (A.7), leading to

$$\frac{\partial\Phi}{\partial n_{\alpha}} \otimes \omega_i^{\alpha} = \mathscr{F}_x^{-1}\mathscr{F}_y^{-1}\mathscr{F}_z^{-1}\left[\widehat{\frac{\partial\Phi}{\partial n_{\alpha}}}(k_x, k_y, k_z)\widehat{\omega}_i^{\alpha}(k_x, k_y, k_z)\right] \tag{20}$$

with the scalar Fourier transform of the partial derivative of the Helmholtz energy density, eq. (A.6), computed according to

$$\widehat{\frac{\partial\Phi}{\partial n_{\alpha}}}(k_x, k_y, k_z) = \mathscr{F}_x \mathscr{F}_y \mathscr{F}_z\left[\frac{\partial\Phi}{\partial n_{\alpha}}(x, y, z)\right] \tag{21}$$

The vector-valued convolution integrals in eq. (10) can be handled using the inverse Fourier transform of scalar-valued functions, eq. (A.7), leading to

$$\begin{aligned} \frac{\partial\Phi}{\partial\mathbf{n}_{\beta}} \otimes \omega_i^{\beta} = \mathscr{F}_x^{-1}\mathscr{F}_y^{-1}\mathscr{F}_z^{-1}\Bigg[&\widehat{\frac{\partial\Phi}{\partial\mathbf{n}_{\beta}}}\Big|_{k_x}\widehat{\omega}_i^{\beta}|_{k_x} + \widehat{\frac{\partial\Phi}{\partial\mathbf{n}_{\beta}}}\Big|_{k_y}\widehat{\omega}_i^{\beta}|_{k_y} \\ &+ \widehat{\frac{\partial\Phi}{\partial\mathbf{n}_{\beta}}}\Big|_{k_z}\widehat{\omega}_i^{\beta}|_{k_z}\Bigg] \end{aligned} \tag{22}$$

where the dot product in Fourier space is used, calculated according to

$$\begin{aligned} \widehat{\frac{\partial\Phi}{\partial\mathbf{n}_{\beta}}} \cdot \widehat{\omega}_i^{\beta} &= \begin{pmatrix} \widehat{\frac{\partial\Phi}{\partial\mathbf{n}_{\beta}}}\Big|_{k_x} \\ \widehat{\frac{\partial\Phi}{\partial\mathbf{n}_{\beta}}}\Big|_{k_y} \\ \widehat{\frac{\partial\Phi}{\partial\mathbf{n}_{\beta}}}\Big|_{k_z} \end{pmatrix} \cdot \begin{pmatrix} \widehat{\omega}_i^{\beta}|_{k_x} \\ \widehat{\omega}_i^{\beta}|_{k_y} \\ \widehat{\omega}_i^{\beta}|_{k_z} \end{pmatrix} \\ &= \widehat{\frac{\partial\Phi}{\partial\mathbf{n}_{\beta}}}\Big|_{k_x}\widehat{\omega}_i^{\beta}|_{k_x} + \widehat{\frac{\partial\Phi}{\partial\mathbf{n}_{\beta}}}\Big|_{k_y}\widehat{\omega}_i^{\beta}|_{k_y} + \widehat{\frac{\partial\Phi}{\partial\mathbf{n}_{\beta}}}\Big|_{k_z}\widehat{\omega}_i^{\beta}|_{k_z} \end{aligned} \tag{23}$$

whereby the vector-valued weight functions, eq. (15), in Fourier space in each direction are defined as

$$\widehat{\omega}_i^{\beta}|_{k_x}(k_x, k_y, k_z) = -\mathrm{i}\,k_x\widehat{\omega}_i^{\alpha}(k_x, k_y, k_z) \tag{24a}$$

$$\widehat{\omega}_i^{\beta}|_{k_y}(k_x, k_y, k_z) = -\mathrm{i}\,k_y\widehat{\omega}_i^{\alpha}(k_x, k_y, k_z) \tag{24b}$$

$$\widehat{\omega}_i^{\beta}|_{k_z}(k_x, k_y, k_z) = -\mathrm{i}\,k_z\widehat{\omega}_i^{\alpha}(k_x, k_y, k_z) \tag{24c}$$

The vector-valued Fourier transform, eq. (A.11), of the vector-valued derivatives of the reduced Helmholtz energy yields

$$\widehat{\frac{\partial\Phi}{\partial\mathbf{n}_{\beta}}}(k_x, k_y, k_z) = \begin{pmatrix} \mathscr{F}_x\mathscr{F}_y\mathscr{F}_z\left[\frac{\partial\Phi}{\partial\mathbf{n}_{\beta}}|_x(x, y, z)\right] \\ \mathscr{F}_x\mathscr{F}_y\mathscr{F}_z\left[\frac{\partial\Phi}{\partial\mathbf{n}_{\beta}}|_y(x, y, z)\right] \\ \mathscr{F}_x\mathscr{F}_y\mathscr{F}_z\left[\frac{\partial\Phi}{\partial\mathbf{n}_{\beta}}|_z(x, y, z)\right] \end{pmatrix} \tag{25}$$

3.2. Convolution in cylindrical coordinates

We regard problems in cylindrical coordinates with angular symmetry, leading to two-dimensional problems. The presented formalism follows Boţan et al. [18], but instead of separating the external potential to obtain vanishing boundary conditions, we separate the density profile directly. The fast Hankel transform algorithm used for computing the Fourier transform requires the function to vanish for large values of the radial coordinate r. That is why we decompose the density profile into a part that approaches zero at large $r = r_{\max}$ and a part that only depends on the axial coordinate according to

$$\rho_i(r, z) = \rho_i^{\Delta}(r, z) + \rho_i^{\infty}(z) \tag{26}$$

The contribution that shifts the density profiles is defined at the r-boundary $\rho_i^{\infty}(z) \equiv \rho_i(r = r_{\max},\ z)$. The remaining contribution $\rho_i^{\Delta}(r, z)$ is well-behaved for a treatment with the fast Hankel

transform.

The Fourier transform of the density profiles is computed according to eq. (A.26) as presented in Appendix A

$$\widehat{\rho}_i(k_r,k_z) = \mathscr{F}_z\mathscr{H}_0\left[\rho_i^{\Delta}(r,z)\right] + \mathscr{F}_z\left[\rho_i^{\infty}(z)\right]\frac{\delta(k_r)}{2\pi k_r} \tag{27}$$

with the Hankel transform of order zero $\mathscr{H}_0$. The solely z-dependent contribution ρ_i^{∞} is transformed via a Fourier transform in z-direction, while the analytical Hankel transform in the constant r-direction yields $\frac{\delta(k_r)}{2\pi k_r}$.

The scalar-valued weighted densities n_a, are calculated using the inverse Fourier transform for scalar functions, eq. (A.27), leading to

$$\begin{aligned} n_\alpha(r,z) \quad &= \sum_{i=1}^{N_c}\Big(\mathscr{F}_z^{-1}\mathscr{H}_0^{-1}\left[\widehat{\rho}_i^{\Delta}(k_r,k_z)\widehat{\omega}_i^{\alpha}(k_r,k_z)\right] \\ &\quad +\mathscr{F}_z^{-1}\left[\widehat{\rho}^{\infty}\left(k_z\right)\widehat{\omega}_i^{\alpha}\left(k_r=0,k_z\right)\right]\Big) \end{aligned} \tag{28}$$

For the vector-valued weighted densities we use the vector-valued weight functions from eq. (15). The inverse Fourier transform is obtained as

$$\begin{aligned} \mathbf{n}_\beta(r,z) \quad = \quad & \sum_{i=1}^{N_c}\left(\begin{pmatrix} \mathscr{F}_z^{-1}\mathscr{H}_1^{-1}\left[k_r\ \widehat{\omega}_i^{\alpha}(k_r,k_z)\widehat{\rho}_i^{\Delta}(k_r,k_z)\right] \\ 0 \\ \mathscr{F}_z^{-1}\mathscr{H}_0^{-1}\left[-\mathrm{i}\ k_z\ \widehat{\omega}_i^{\alpha}(k_r,k_z)\widehat{\rho}_i^{\Delta}(k_r,k_z)\right] \end{pmatrix}\right. \\ & \left.+\begin{pmatrix} 0 \\ 0 \\ \mathscr{F}_z^{-1}\left[-\mathrm{i}\ k_z\ \widehat{\omega}_i^{\alpha}(k_r=0,k_z)\widehat{\rho}_i^{\infty}(k_z)\right] \end{pmatrix}\right) \end{aligned} \tag{29}$$

with the Hankel transform of zeroth and first order, $\mathscr{H}_0$ and $\mathscr{H}_1$, respectively. For this result we made use of the inverse Fourier transform for vector-valued functions, eq. (A.42). The convolution integrals of the Helmholtz energy density derivatives $\frac{\partial\Phi}{\partial n_{\alpha,\beta}}$ with the weight functions $\omega_i^{\alpha,\beta}$ are computed similarly. The partial derivatives $\frac{\partial\Phi}{\partial n_{\alpha,\beta}}$ at the r-boundary do not approach zero in general. Analogous to eq. (26) we therefore shift the profile by splitting the partial derivatives into a r- and z-dependent contribution $\frac{\partial\Phi^{\Delta}}{\partial n_{\alpha,\beta}}(r,z)$, which approaches zero at the r-boundary, and the z-dependent value at the r-boundary $\frac{\partial\Phi^{\infty}}{\partial n_{\alpha,\beta}}(z)$, according to

$$\frac{\partial\Phi}{\partial n_{\alpha,\beta}}(r,z) = \frac{\partial\Phi^{\Delta}}{\partial n_{\alpha,\beta}}(r,z) + \frac{\partial\Phi^{\infty}}{\partial n_{\alpha,\beta}}(z) \tag{30}$$

For the scalar terms one obtains

$$\begin{aligned} \frac{\partial\Phi}{\partial n_\alpha}\otimes\omega_i^{\alpha} = \ & \mathscr{F}_z^{-1}\mathscr{H}_0^{-1}\left[\widehat{\frac{\partial\Phi^{\Delta}}{\partial n_\alpha}}(k_r,k_z)\widehat{\omega}_i^{\alpha}(k_r,k_z)\right] \\ & +\mathscr{F}_z^{-1}\left[\widehat{\frac{\partial\Phi^{\infty}}{\partial n_\alpha}}(k_z)\widehat{\omega}_i^{\alpha}(k_r=0,k_z)\right] \end{aligned} \tag{31}$$

using the scalar inverse Fourier transform from eq. (A.27). With the scalar Fourier transform of the partial derivative of the Helmholtz energy density, eq. (A.26), according to

$$\widehat{\frac{\partial\Phi}{\partial n_\alpha}}(k_r,k_z) = \mathscr{F}_z\mathscr{H}_0\left[\frac{\partial\Phi^{\Delta}}{\partial n_\alpha}(r,z)\right] + \mathscr{F}_z\left[\frac{\partial\Phi^{\infty}}{\partial n_\alpha}(z)\right]\frac{\delta(k_r)}{2\pi k_r} \tag{32}$$

For the vector-valued contributions we have

$$\frac{\partial\Phi}{\partial\mathbf{n}_\beta}\otimes\omega_i^{\beta} = \mathscr{F}_z^{-1}\mathscr{H}_0^{-1}\left[\widehat{\frac{\partial\Phi}{\partial\mathbf{n}_\alpha}}\Big|_{k_r}\widehat{\omega}_i^{\alpha}|_{k_r} + \widehat{\frac{\partial\Phi}{\partial\mathbf{n}_\alpha}}\Big|_{k_z}\widehat{\omega}_i^{\alpha}|_{k_z}\right] \tag{33}$$

where the expression in angular brackets results from the dot product in Fourier space

$$\widehat{\frac{\partial\Phi}{\partial\mathbf{n}_\beta}}\cdot\widehat{\omega}_i^{\beta} = \begin{pmatrix} \widehat{\frac{\partial\Phi}{\partial\mathbf{n}_\beta}}\Big|_{k_r} \\ 0 \\ \widehat{\frac{\partial\Phi}{\partial\mathbf{n}_\beta}}\Big|_{k_z} \end{pmatrix}\cdot\begin{pmatrix} \widehat{\omega}_i^{\beta}|_{k_r} \\ 0 \\ \widehat{\omega}_i^{\beta}|_{k_z} \end{pmatrix} = \widehat{\frac{\partial\Phi}{\partial\mathbf{n}_\beta}}\Big|_{k_r}\widehat{\omega}_i^{\beta}|_{k_r} + \widehat{\frac{\partial\Phi}{\partial\mathbf{n}_\beta}}\Big|_{k_z}\widehat{\omega}_i^{\beta}|_{k_z} \tag{34}$$

requiring the weight functions from eq. (15)

$$\widehat{\omega}_i^{\beta}|_{k_r}(k_r,k_z) = -\mathrm{i}\,k_r\widehat{\omega}_i^{\alpha}(k_r,k_z) \tag{35a}$$

$$\widehat{\omega}_i^{\beta}|_{k_z}(k_r,k_z) = -\mathrm{i}\,k_z\widehat{\omega}_i^{\alpha}(k_r,k_z) \tag{35b}$$

using the inverse Fourier transform for scalar functions from eq. (A.27). Equation (33) further requires the vector-valued Fourier transform, eq. (A.35), of the vector-valued derivatives

$$\begin{aligned} \widehat{\frac{\partial\Phi}{\partial\mathbf{n}_\beta}}(k_r,k_z) = & \begin{pmatrix} \mathscr{F}_z\mathscr{H}_1\left[-\mathrm{i}\ \frac{\partial\Phi^{\Delta}}{\partial\mathbf{n}_\beta}|_r(r,z)\right] \\ 0 \\ \mathscr{F}_z\mathscr{H}_0\left[\frac{\partial\Phi^{\Delta}}{\partial\mathbf{n}_\beta}|_z(r,z)\right] \end{pmatrix} \\ & +\begin{pmatrix} 0 \\ 0 \\ \mathscr{F}_z\left[\frac{\partial\Phi^{\infty}}{\partial\mathbf{n}_\beta}(z)\right]\frac{\delta(k_r)}{2\pi k_r} \end{pmatrix} \end{aligned} \tag{36}$$

Combining eqs. (35) and (36) in eq. (33) we obtain for the vector-valued contributions

$$\begin{aligned} \frac{\partial\Phi}{\partial\mathbf{n}_\beta}\otimes\omega_i^{\beta} \quad = \quad & \mathscr{F}_z^{-1}\mathscr{H}_0^{-1}\Big[-\mathrm{i}\,\widehat{\omega}_i^{\alpha}(k_r,k_z) \\ & \times\left(k_r\widehat{\frac{\partial\Phi^{\Delta}}{\partial\mathbf{n}_\beta}}|_{k_r}(k_r,k_z) + k_z\widehat{\frac{\partial\Phi^{\Delta}}{\partial\mathbf{n}_\beta}}|_{k_z}(k_r,k_z)\right)\Big] \\ & +\mathscr{F}_z^{-1}\left[-\mathrm{i}\ k_z\ \widehat{\omega}_i^{\alpha}(k_r=0,k_z)\widehat{\frac{\partial\Phi^{\infty}}{\partial\mathbf{n}_\beta}}|_{k_z}(k_z)\right] \end{aligned} \tag{37}$$

3.3. Convolution in spherical coordinates

The fast sine/cosine transform algorithms used for computing the Fourier transform in spherical coordinates require the function to vanish for large values of r. If the density profiles $\rho_i(r)$ do not approach zero, we define shifted profiles $\rho_i^{\Delta}(r)$ which do approach zero at large radial distances $r = r_{\max}$ by splitting the density profile

$$\rho_i(r) = \rho_i^{\Delta}(r) + \rho_i^{\infty} \tag{38}$$

into a r-dependent contribution $\rho_i^{\Delta}(r)$, vanishing at the boundary, and the constant value at the boundary $\rho_i^{\infty}(r = r_{\max})$. The Fourier transform of the density profiles is computed as presented in Appendix A, according to eq. (A.52) while the constant boundary value can be computed analytically, leading to

$$\widehat{\rho}_i(k_r) = \frac{2}{k_r}\mathscr{SIN}\left[\rho_i^{\Delta}(r)\, r\right] + \rho_i^{\infty}\delta(k_r) \tag{39}$$

The scalar-valued weighted densities n_a, are then calculated based on the inverse Fourier transform for scalar functions, eq. (A.53), leading to

$$n_\alpha(r) = \sum_{i=1}^{N_c}\left(\frac{2}{r}\mathscr{SIN}\left[k_r\, \widehat{\omega}_i^{\alpha}(k_r)\widehat{\rho}_i^{\Delta}(k_r)\right] + \widehat{\omega}_i^{\alpha}(k_r = 0)\rho_i^{\infty}\right) \tag{40}$$

For the vector-valued weighted densities we use the vector-valued weight functions, eq. (15), and transform them back to real space using the inverse Fourier transform for vector-valued functions from eq. (A.71). For the vector-valued weight functions

$$\begin{aligned}\mathbf{n}_\beta(r) \;=\; & \sum_{i=1}^{N_c}\left(\mathbf{e}_r\frac{\mathrm{i}}{\pi r^2}\mathscr{SIN}\left[-\mathrm{i}\; k_r\; \widehat{\omega}_i^{\alpha}\left(k_r\right)\widehat{\rho}_i^{\Delta}\left(k_r\right)\right]\right. \\ & \left.-\mathbf{e}_r\frac{2\mathrm{i}}{r}\mathscr{COS}\left[-\mathrm{i}\; k_r\; \widehat{\omega}_i^{\alpha}\left(k_r\right)\, k_r\widehat{\rho}_i^{\Delta}\left(k_r\right)\right]\right)\end{aligned} \tag{41}$$

the convolution with the constant value from shifting the density profile vanishes due to $\widehat{\omega}_i^{\beta}(k_r = 0) = 0$. The convolution integrals of the Helmholtz energy density derivatives $\frac{\partial\Phi}{\partial n_{\alpha,\beta}}$ with the weight functions $\omega_i^{\alpha,\beta}$ are computed similarly. If the partial derivatives $\frac{\partial\Phi}{\partial n_{\alpha,\beta}}$ do not vanish, we shift the profile to zero by splitting the partial derivatives into a r-dependent contribution $\frac{\partial\Phi^{\Delta}}{\partial n_{\alpha,\beta}}(r)$, vanishing at the boundary, and the constant value at the boundary $\frac{\partial\Phi^{\infty}}{\partial n_{\alpha,\beta}}$ according to

$$\frac{\partial\Phi}{\partial n_{\alpha,\beta}}(r) = \frac{\partial\Phi^{\Delta}}{\partial n_{\alpha,\beta}}(r) + \frac{\partial\Phi^{\infty}}{\partial n_{\alpha,\beta}} \tag{42}$$

For the scalar terms one obtains

$$\frac{\partial\Phi}{\partial n_\alpha}\otimes\omega_i^{\alpha} = \frac{2}{r}\mathscr{SIN}\left[\widehat{\frac{\partial\Phi^{\Delta}}{\partial n_\alpha}}(k_r)\widehat{\omega}_i^{\alpha}(k_r)\, k_r\right] + \frac{\partial\Phi^{\infty}}{\partial n_\alpha}\widehat{\omega}_i^{\alpha}(k_r = 0) \tag{43}$$

using the scalar inverse Fourier transform from eq. (A.53). With the scalar Fourier transform of the partial derivative of the Helmholtz energy density, eq. (A.52), obtained from

$$\widehat{\frac{\partial\Phi}{\partial n_\alpha}}(k_r) = \frac{2}{k_r}\mathscr{SIN}\left[\frac{\partial\Phi^{\Delta}}{\partial n_\alpha}(r)\, r\right] + \frac{\partial\Phi^{\infty}}{\partial n_\alpha}\delta(k_r) \tag{44}$$

For the vector-valued derivatives we compute the dot product

$$\begin{aligned}\widehat{\frac{\partial\Phi}{\partial\mathbf{n}_\beta}}\cdot\widehat{\omega}_i^{\beta} \;&=\; \left.\widehat{\frac{\partial\Phi^{\Delta}}{\partial\mathbf{n}_\beta}}\right|_{k_r}\mathbf{e}_{k_r}\cdot\widehat{\omega}_i^{\beta}|_{k_r}\mathbf{e}_{k_r} + \frac{\partial\Phi^{\infty}}{\partial\mathbf{n}_\beta}|_{k_r}\delta(k_r)\mathbf{e}_{k_r}\cdot\widehat{\omega}_i^{\beta}|_{k_r}\mathbf{e}_{k_r} \\ &=\; \left.\widehat{\frac{\partial\Phi^{\Delta}}{\partial\mathbf{n}_\beta}}\right|_{k_r}\widehat{\omega}_i^{\beta}|_{k_r} + \frac{\partial\Phi^{\infty}}{\partial\mathbf{n}_\beta}|_{k_r}\delta(k_r)\widehat{\omega}_i^{\beta}|_{k_r}\end{aligned} \tag{45}$$

in Fourier space, the convolution with the constant value from shifting the density profile vanishes due to $\widehat{\omega}_i^{\beta}(k_r = 0) = 0$. The weight functions, eq. (15), are obtained from

$$\widehat{\omega}_i^{\beta}|_{k_r}(k_r) = -\,\mathrm{i}\, k_r\widehat{\omega}_i^{\alpha}(k_r) \tag{46}$$

In real space, this results in

$$\frac{\partial\Phi}{\partial\mathbf{n}_\beta}\otimes\omega_i^{\beta} = \frac{2}{r}\mathscr{SIN}\left[\left.\widehat{\frac{\partial\Phi^{\Delta}}{\partial\mathbf{n}_\beta}}\right|_{k_r}\widehat{\omega}_i^{\beta}|_{k_r}k_r\right] \tag{47}$$

with the inverse Fourier transform for scalar functions, eq. (A.53). With the vector-valued Fourier transform, eq. (A.62), of the vector-valued derivatives obtained from

$$\begin{aligned}\widehat{\frac{\partial\Phi}{\partial\mathbf{n}_\beta}}(k_r) \;&=\; \mathbf{e}_{k_r}\frac{2\mathrm{i}}{k_r}\mathscr{COS}\left[\frac{\partial\Phi^{\Delta}}{\partial\mathbf{n}_\beta}|_r(r)\, r\right] \\ &\quad -\mathbf{e}_{k_r}\frac{\mathrm{i}}{\pi k_r^2}\mathscr{SIN}\left[\frac{\partial\Phi^{\Delta}}{\partial\mathbf{n}_\beta}|_r(r)\right] + \mathbf{e}_{k_r}\frac{\partial\Phi^{\infty}}{\partial\mathbf{n}_\beta}|_{k_r}\delta(k_r)\end{aligned} \tag{48}$$

Combining the above equations for the vector-valued convolution, we obtain

$$\frac{\partial\Phi}{\partial\mathbf{n}_\beta}\otimes\omega_i^{\beta} = \frac{2}{r}\mathscr{SIN}\left[-\,\mathrm{i}\, k_r\widehat{\omega}_i^{\alpha}(k_r)\left.\widehat{\frac{\partial\Phi^{\Delta}}{\partial\mathbf{n}_\beta}}\right|_{k_r}k_r\right] \tag{49}$$

4. From integral transform to discretized representation

In this section we discuss the transition from continuous integral transforms to discrete representations of the inhomogeneous field variables (e.g. ρ_i). For Cartesian coordinates, the fast Fourier transform is used. For cylindrical coordinates we apply a combination of the fast Fourier and the fast Hankel transform (from a combination of fast Abel and fast Fourier transform, appearing as fast sine and cosine transform). For spherical coordinates the fast sine and cosine transforms are utilized. Because the weight functions from the weighted density approaches ω_i are transformed to Fourier space analytically, we also show the connection of the **r**-grid in real space to the **k**-grid in Fourier space. The fast Fourier, fast sine and fast cosine transforms are taken from *FFTPACK* [55,56], while the fast Abel transform follows Hansen [53] and Hansen and Law [54], described in detail in Appendix C. Strategies to minimize Gibbs phenomenon are presented in Appendix E.

4.1. Cartesian grid

For Cartesian coordinates, we use the FFT in each dimension. A schematic grid is visualized in Fig. 1. FFT algorithms require real space samples evaluated on an equidistant grid. Even though a physical problem may be non-periodic in the domain of interest $L_{\mathrm{in},z}$, fast Fourier transforms will treat the considered domain as is it

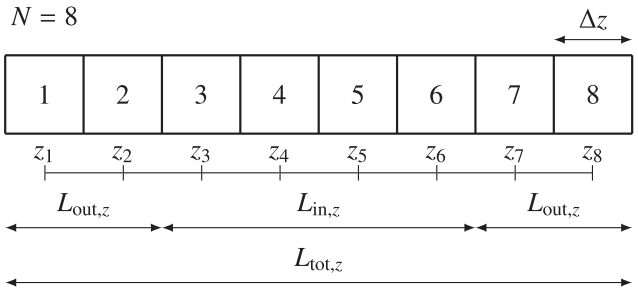

Fig. 1. Schematic equidistant Cartesian grid with $N = 8$ grid points and grid spacing Δz. The partitioned elements represent a discretization used for finite volume methods, while the function to be transformed is evaluated at the center of those elements z_i. The density profiles are computed on the inner domain $L_{\text{in},z}$, while the buffer zones $L_{\text{out},z}$ compensate the periodic continuation of the FFT and serve as boundary conditions.

was surrounded by infinitely many (i.e. periodic) images of itself. To suppress the unwanted effect of periodic copies of the regarded domain, definition of a buffer region $L_{\text{out},z}$ on each side of the domain is needed. The two outer buffer regions $L_{\text{out},z}$ also serve as constant boundary conditions for the evaluation of the weighted densities at the boundary. Due to the functional nature of the problem a buffer domain is required as boundary condition, in contrast to boundary conditions for functions where information about a single point is sufficient.

4.1.1. Grid and boundary conditions

We thus consider a grid covering three domains, the two outer buffer domains with length $L_{\text{out},z}$, and the inner domain of interest with length $L_{\text{in},z}$, where the density profiles are iterated. To better connect this section to the previous one, we remind that the grand potential functional Ω is a functional of density profiles $\{\rho_i\}$ and a function of the variables $(\{\mu_i\}, T, V)$, whereby the system volume V is defined by the domain length $L_{\text{in},z}$ in z-direction. The choice for the value of the buffer length $L_{\text{out},z}$ is determined by the *influence length* of the weight functions. Here, the weight functions, eq. (6), have an influence length of R_i. For the hard-sphere fluid as described with the modified FMT [57,58], two times the influence length corresponds to the closest approach of two hard spheres of type i. Because two types of convolutions are computed (one for computation of the weighted density profiles and one for the convolution of the reduced Helmholtz energy with the weight functions), the buffer length $L_{\text{out},z}$ has to be at least twice the value of R_i. After each of the two convolutions, a fraction of the buffer domain with length R_i is tainted due to possible inhomogeneous boundary conditions and periodic continuation of the FFT, which leads to the length of the buffer zone, as

$$L_{\text{out},z} \geq \max_i \{2R_i(T)\} \tag{50}$$

4.1.2. Discrete representation for FFT algorithm

We now explain the **k**-grid in Fourier space for the computation of the weight functions, eqs. (14) and (15). The approach is shown for one dimension only. Higher dimensions are the result of multiple consecutive Fourier transforms and can be treated analogously.

The discrete Fourier transform with Fourier variable k as used in FFT algorithms is defined as the following sum

$$\widehat{f}_k = \sum_{j=0}^{N-1} f_j \, \mathrm{e}^{-2\pi \mathrm{i} \frac{jk}{N}} \qquad \text{with } k = 0, \cdots, (N-1) \tag{51}$$

which transforms a finite series of N equally-spaced samples $z_j = j\,\Delta z$ of a function f_j into a series of equally-spaced samples of the function in Fourier space $\widehat{f}_k$. Index j denotes the discrete grid points in real space, while k denotes the grid points in Fourier space.

In comparison, the continuous Fourier transform can be discretized as well with $z_j = j\Delta z$ and $f(z_j) = f_j$. The continuous Fourier transform then leads to a similar equation as the discretization of the Fourier transform, eq. (51), namely to

$$\widehat{f}(k_z) = \int_{z=-\infty}^{\infty} f(z) \, \mathrm{e}^{-2\pi \mathrm{i}\, z k_z} \, \mathrm{d}z \approx \sum_{j=0}^{N-1} f_j \, \mathrm{e}^{-2\pi \mathrm{i}\, j \Delta z k_z} \Delta z \tag{52}$$

where the result is multiplied with Δz compared to the unscaled version in eq. (51). Comparison of the arguments of the exponential functions in eqs. (51) and (52) $\frac{jk}{N} = j\Delta z k_z$ yields the discretization in Fourier space, as

$$k_z = \frac{k}{N\Delta z} = \frac{k}{L_{\text{tot},z}} \qquad \text{with } k = 0, \cdots, (N-1) \tag{53}$$

At first glance, this result differs from the one proposed by Knepley et al. [1], because we define $L_{\text{tot},z}$ differently. We evaluate the function to be transformed at the center of the elements in Fig. 1 instead of the edges, as done by Knepley et al. [1], so that the regarded overall domain for the work of Knepley et al. ($\tilde{L}_{\text{tot},z} = L_{\text{tot},z} - \Delta z$) is different to our overall domain length ($L_{\text{tot},z}$) for the same number of grid points N and the same discretization step size Δz. Complex-valued FFT algorithms include negative k-values as well. For an even number of grid points, the k-vector for the computation of the discrete representation of the weight functions, eqs. (14) and (15), is

$$k_z = \frac{1}{L_{\text{tot},z}} \left[0, 1, \cdots, \left(\frac{N}{2} - 1\right), \left(-\frac{N}{2}\right), \cdots, -1\right] \tag{54}$$

For real-valued FFT algorithms, the k-vector looks differently

$$k_z = \frac{1}{L_{\text{tot},z}} \left[0, 1, 1, 2, 2, \cdots, \left(\frac{N}{2}\right)\right] \tag{55}$$

this yields a k_z-grid in Fourier space which is used for the analytical computation of the weight functions $\widehat{\omega}_i$, eq. (14) and (15). These weight functions $\widehat{\omega}_i$ are then multiplied in Fourier space with the FFT output of the function to be convolved, the result of which is transformed back to real space using the inverse FFT. For higher dimensions, the k-grid becomes a two- or three-dimensional array, while k_x and k_y are constructed equivalently to eq. (54) or eq. (55) with their respective length scale $L_{\text{tot},x}$ and $L_{\text{tot},y}$. The absolute value of **k** is calculated as

$$|\mathbf{k}| = \sqrt{k_x^2 + k_y^2 + k_z^2} \tag{56}$$

4.2. Cylindrical grid

For cylindrical coordinates, we use the fast Fourier in axial and the fast Hankel transform (as a combination of fast Abel and fast sine and cosine transform) in radial direction. The procedure of the axial direction is equivalent to the approach for Cartesian

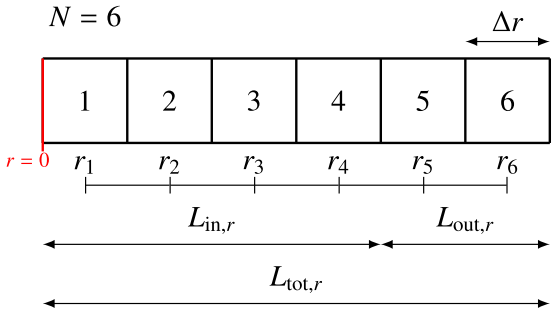

Fig. 2. Schematic equidistant radial grid with $N = 6$ grid points and grid spacing Δr. The partitioned elements represent a discretization used for finite volume methods, while the function to be transformed is evaluated at the center of those elements r_i. The density profiles are computed on the inner domain $L_{\text{in},r}$, while the buffer zone $L_{\text{tot},r}$ serves as boundary condition, where the density profiles ρ_i^{Δ} go to zero.

coordinates as described in the previous section, therefore, only the radial direction is regarded here. A schematic grid is visualized in Fig. 2. As opposed to the approach of Boţan et al. [18], who computed discrete Hankel transform on a logarithmic grid, we adopt the ideas of Hansen [52,53] and Hansen and Law [54], using a combination of Abel and Fourier transforms, which allows computation of the Hankel transform on equidistant grids.

4.2.1. Grid and boundary conditions

The radial grid is divided into two domains, the outer domain with length $L_{\text{out},r}$, which is needed as boundary condition for the evaluation of the weighted densities at the boundary, and the inner domain with length $L_{\text{in},r}$, where the density profiles are iterated. Due to even and odd continuation of the fast sine and fast cosine transform, respectively, no boundary domain for $r < 0$ is needed. The size of the outer domain $L_{\text{out},r}$ is determined as described in section 4.1.1. Therefore, the size of the outer domain is determined as

$$L_{\text{out},r} \geq \max_i \{2R_i(T)\} \tag{57}$$

4.2.2. Discrete representation for FFT and fast hankel transform algorithms

The **k**-grid in Fourier space for the computation of the weight functions, eqs. (14) and (15), is computed as follows. The axial direction is equivalent to the Cartesian grid, eq. (53), whereas for the radial component the k-values correspond to twice the domain shown in Fig. 2. Instead of the Fourier, the discrete sine and cosine transform are used, which exploit symmetry and, therefore, require only half of the Fourier domain. The length of the whole Fourier domain in radial direction is $(2L_{\text{tot},r})$. This leads to the following k-grid for the radial component

$$k_r = \frac{k}{2N\Delta r} = \frac{k}{2L_{\text{tot},r}} \qquad \text{with } k = 0, \cdots, (N-1) \tag{58}$$

This yields a k_r-grid in Fourier space which, together with the k_z-grid, is used for the analytical computation of the weight functions $\hat{\omega}_i$, eqs. (14) and (15). These weight functions $\hat{\omega}_i$ are then multiplied in Fourier space with the FFT and fast Hankel transform output of the function to be convolved, and this result can be transformed back to real space using the inverse FFT and inverse fast Hankel transform algorithms. For two dimensional problems in cylindrical coordinates, the **k**-grid becomes a two-dimensional array. The absolute value of **k** is calculated as

$$|\mathbf{k}| = \sqrt{k_r^2 + k_z^2} \tag{59}$$

In this work, we utilize the projection-slice theorem for the computation of the Hankel transform, where the Hankel transform is replaced by

$$\mathscr{H}_0[f(r)] = \mathscr{F}_r \mathscr{A}[f(r)] \tag{60}$$

a combination of Fourier $\mathscr{F}$ and Abel transform $\mathscr{A}$. The algorithm for computation of the fast Hankel transform is based on work of Hansen [52] and described in detail in Appendix C. The inverse transform is computed from a combination of inverse Abel and inverse Fourier transform, as

$$\mathscr{H}_0^{-1}\left[\widehat{f}(k_r)\right] = \mathscr{A}^{-1}\mathscr{F}_r^{-1}\left[\widehat{f}(k_r)\right] \tag{61}$$

The Abel transform is computed as described in Appendix C. As a result of rotational symmetry, all density profiles are even with respect to $r = 0$. This allows using the cosine instead of the Fourier transform. Because some calculations require a division by the radius r, we locate the first grid point at $r = \frac{\Delta r}{2}$. For this grid distribution, we require the discrete cosine transform II ($\mathscr{DCT}_{\text{II}}$) which is available in *FFTPACK* as subroutine *COSQ1B*. More details on the discrete cosine transform are presented in Appendix D. The Fourier transform of scalar functions $f(r, z)$, using the Hankel transform of zeroth order as in eq. (A.26), is computed from

$$\widehat{f}(k_r, k_z) = \mathscr{F}_z\, \mathscr{DCT}_{\text{II}}\, \mathscr{A}[f(r,z)] \tag{62}$$

with the Abel transform $\mathscr{A}$. The inverse transform uses the discrete cosine transform III ($\mathscr{DCT}_{\text{III}} = \mathscr{DCT}_{\text{II}}^{-1}$) which is available in *FFTPACK* as subroutine *COSQ1F* and can be computed via

$$f(r,z) = \mathscr{A}^{-1}\, \mathscr{DCT}_{\text{III}}\, \mathscr{F}_z^{-1}\left[\widehat{f}(k_r, k_z)\right] \tag{63}$$

For vector-valued functions, the Hankel transform of first order is computed from the zeroth order Hankel transform with eq. (B.3) from Appendix B, leading to

$$\begin{aligned} \widehat{f}(k_r, k_z)|_{k_r} &= \mathscr{F}_z \mathscr{H}_1[f(r,z)|_r] \\ &= \mathscr{F}_z\left[\frac{1}{2\pi k_r}\, \mathscr{DCT}_{\text{II}} \mathscr{A}\left[\frac{f(r,z)|_r}{r} + \frac{\partial f(r,z)|_r}{\partial r}\right]\right] \end{aligned} \tag{64}$$

The application of this is limited to the radial contribution in eq. (36), where $f(r,z)|_r = -\mathrm{i}\, \frac{\partial \Phi^{\Delta}}{\partial \mathbf{n}_\beta}|_r(r,z)$ is an odd function in r. This leads to the derivative $\frac{\partial f(r,z)|_r}{\partial r}$ being an even function. Even continuation of the $\mathscr{DCT}_{\text{II}}$ allows neglecting the odd contribution $\frac{f(r,z)|_r}{r}$, which leads to the simpler form

$$\widehat{f}(k_r, k_z)|_{k_r} = \mathscr{F}_z\left[\frac{1}{2\pi k_r}\, \mathscr{DCT}_{\text{II}} \mathscr{A}\left[\frac{\partial f(r,z)|_r}{\partial r}\right]\right] \tag{65}$$

The derivative $\frac{\partial f(r,z)}{\partial r}$ can be approximated using central differences with vanishing boundary conditions from

$$\frac{\partial f\left(z, r^{(n)}\right)}{\partial r} \approx \frac{f\left(r^{(n+1)}, z\right) - f\left(r^{(n-1)}, z\right)}{r^{(n+1)} - r^{(n-1)}} \tag{66}$$

The inverse transform is computed similarly, according to

$$
\begin{aligned}
f(r,z)|_r &= \mathscr{H}_1^{-1}\mathscr{F}_z^{-1}\left[\widehat{f}(k_r,k_z)|_{k_r}\right] \\
&= \frac{1}{r}\mathscr{H}_0^{-1}\left[\frac{\mathscr{F}_z^{-1}\left[\widehat{f}(k_r,k_z)|_{k_r}\right]}{2\pi k_r}+\frac{\partial\mathscr{F}_z^{-1}\left[\widehat{f}(k_r,k_z)|_{k_r}\right]}{\partial k_r}\right] \\
&= \frac{1}{r}\mathscr{A}^{-1}\mathscr{F}_r^{-1}\left[\frac{\mathscr{F}_z^{-1}\left[\widehat{f}(k_r,k_z)|_{k_r}\right]}{2\pi k_r}+\frac{\partial\mathscr{F}_z^{-1}\left[\widehat{f}(k_r,k_z)|_{k_r}\right]}{\partial k_r}\right]
\end{aligned}
\tag{67}
$$

The derivative in the second term of eq. (67) can be replaced using the identity

$$
\mathscr{F}_r^{-1}\left[\frac{\partial\widehat{g}(k_r,z)}{\partial k_r}\mathrm{i}\right]=2\pi r\mathscr{F}_r^{-1}[\widehat{g}(k_r,z)] \tag{68}
$$

with $\widehat{g}(k_r,z)=\mathscr{F}_z^{-1}[\widehat{f}(k_r,k_z)|_{k_r}]$. This is applied to eq. (29) where $\widehat{g}(k_r,z)$ is a real even function in k_r, making $\left(\frac{\partial\widehat{g}(k_r,z)}{\partial k_r}\mathrm{i}\right)$ purely imaginary and odd in k_r. The purely imaginary and odd inverse Fourier transform $\mathscr{F}_r^{-1}\left[\frac{\partial\widehat{g}(k_r,z)}{\partial k_r}\mathrm{i}\right]$ can, therefore, be replaced by the sine transform $2\pi r\mathscr{DST}_{\mathrm{III}}[\widehat{g}(k_r,z)]$. The first term in eq. (67) transforms an even function and allows for replacing the Fourier transform $\mathscr{F}_r^{-1}$ with the $\mathscr{DCT}_{\mathrm{III}}$, according to

$$
\begin{aligned}
f(r,z)|_r &= \frac{1}{r}\mathscr{A}^{-1}\left[\mathscr{DCT}_{\mathrm{III}}\mathscr{F}_z^{-1}\left[\frac{\widehat{f}(k_r,k_z)|_{k_r}}{2\pi k_r}\right]\right. \\
&\quad \left.+2\pi r\mathscr{DST}_{\mathrm{III}}\mathscr{F}_z^{-1}\left[\widehat{f}(k_r,k_z)|_{k_r}\right]\right]
\end{aligned}
\tag{69}
$$

Equation (65) with eq. (66) and (69) are our final equations for the forward and inverse transform in radial direction, respectively.

Here we require the discrete sine transform III ($\mathscr{DST}_{\mathrm{III}}$) which is available in *FFTPACK* as subroutine *SINQ1F*. The grid for the $\mathscr{DST}_{\mathrm{III}}$ algorithm has to be shifted in Fourier space. The procedure is described in section 4.3.2 and visualized in Fig. 5. More details on the discrete sine and cosine transform are presented in Appendix D.

4.3. Spherical grid

In spherical coordinates we only consider one-dimensional problems, where angular symmetry exists. We use the fast sine and fast cosine transform. A schematic grid is visualized in Fig. 3. Fast sine and cosine transform algorithms require real space samples evaluated on an equidistant grid.

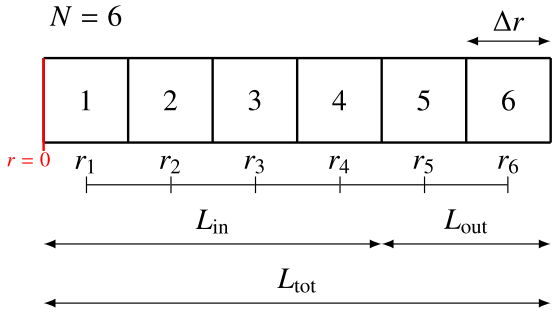

Fig. 3. Schematic equidistant spherical grid with $N=6$ grid points and grid spacing Δr. The partitioned elements represent a discretization used for finite volume methods, while the function to be transformed is evaluated at the center of those elements r_i. The density profiles are computed on the inner domain L_{in}, while the buffer zone L_{out} compensates for periodic continuation of the fast sine and cosine transform, and serves as boundary condition, where the density profiles ρ_i^{Δ} go to zero.

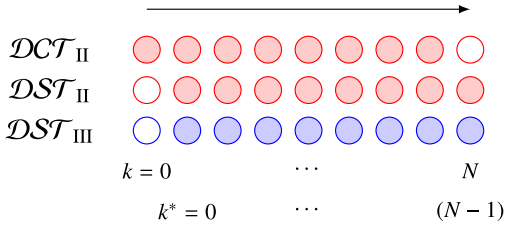

Fig. 4. Shift of indices to match $\mathscr{DST}_{\mathrm{II}}$ and $\mathscr{DCT}_{\mathrm{II}}$ to $\mathscr{DST}_{\mathrm{III}}$. Filled spheres represent the k-grid of the respective forward (red) and inverse (blue) transform.

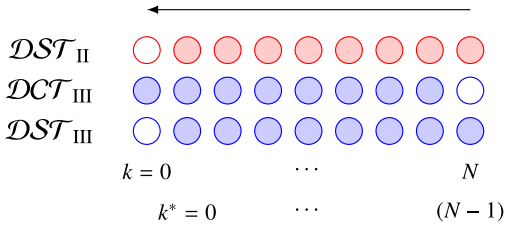

Fig. 5. Shift of indices to match $\mathscr{DST}_{\mathrm{II}}$ and $\mathscr{DCT}_{\mathrm{III}}$ to $\mathscr{DST}_{\mathrm{II}}$. Filled spheres represent the k-grid of the respective forward (red) and inverse (blue) transform.

4.3.1. Grid and boundary conditions

Similar to cylindrical coordinates, no boundary domain for $r<0$ is needed, because the used algorithms for the discrete sine and cosine transform assume odd and even continuation, respectively, which can be exploited here due to spherical symmetry requirements. The size of the outer domain L_{out} is determined as described in section 4.1.1. Therefore, the size of the outer domain is determined as

$$
L_{\mathrm{out}} \geq \max_i\{2R_i(T)\} \tag{70}
$$

4.3.2. Discrete representation for sine and cosine transform algorithms

The **k**-grid in Fourier space for the computation of the weight functions, eqs. (14) and (15), is computed as follows. The discrete sine and cosine transform are recovered by discretization of the derived Fourier transform in spherical coordinates. There are four relevant variants of the sine and cosine transform, each with a set of different boundary conditions and discretization schemes. Due to the singularity at the origin in spherical coordinates, we locate the first grid point at $r=\frac{\Delta r}{2}$. For this grid distribution, we need the discrete sine transform II ($\mathscr{DST}_{\mathrm{II}}$), according to

$$
\widehat{f}_{k^*}=\sum_{j=0}^{N-1}f_j\sin\left[\frac{\pi}{N}\left(j+\frac{1}{2}\right)(k^*+1)\right] \tag{71}
$$

$$
\text{with } k^*=0,\cdots,(N-1)
$$

which is available in *FFTPACK* as subroutine *SINQ1B*. More details on the discrete sine transform are presented in Appendix D. The iteration variable k^* does not represent the true Fourier variable k, which for the $\mathscr{DST}_{\mathrm{II}}$ is obtained from $k=k^*+1$.

The matching discrete cosine transform is the $\mathscr{DCT}_{II}$, computed as

$$\widehat{f}_k = \sum_{j=0}^{N-1} f_j \cos\left[\frac{\pi}{N}\left(j+\frac{1}{2}\right)k\right] \quad \text{with } k = 0, \cdots, (N-1) \tag{72}$$

which is available in *FFTPACK* as subroutine *COSQ1B*. More details on the discrete cosine transform are presented in Appendix D. Both transforms transform a finite series of equally-spaced samples $z_j = \frac{1}{N}\left(j+\frac{1}{2}\right)$ of a function f_j into a series of equal length in Fourier space $\widehat{f}_k$. The index j denotes the discrete grid points in real space, while k denotes the grid points in Fourier space.

For both transforms, indices k and k^* run from $0, \cdots, (N-1)$ in Fourier space, but the $\mathscr{DST}_{II}$ treats the point $k = 0$ implicitly as $\widehat{f}_{k=0}^{\mathscr{DST}} = 0$, while the $\mathscr{DCT}_{II}$ treats the value $\widehat{f}_{k=0}^{\mathscr{DCT}}$ explicitly. In contrast, the $\mathscr{DCT}_{II}$ does not provide a value for $k = N$, while the $\mathscr{DST}_{II}$ does (as $k^* = N-1$). Because the transformation to Fourier space in eqs. (41) and (48) requires $f(r)$ to be multiplied with r, the argument of the sine and cosine transform are always zero at $r = 0$, which leads to $\widehat{f}_{k=0}^{\mathscr{DCT}} = 0$.

For the computation of eq. (48) a combination of $\mathscr{DST}_{II}$ and $\mathscr{DCT}_{II}$ is needed. Because the inverse transform, eq. (47), uses solely the $\mathscr{DST}_{III}$ the value $\widehat{f}_{k=0}^{\mathscr{DCT}} = 0$ can be neglected, but the value for $k = N$ (or $k^* = N-1$) for the $\mathscr{DST}_{III}$ has to be added: $\widehat{f}_{k=N}^{\mathscr{DST}} = 0$. This approach is not exact, but a reasonable approximation as $\widehat{f}_{k\to\infty}^{\mathscr{DCT}} \to 0$ for smooth functions and appropriate number of grid points. This procedure is necessary to match the different k-values of the $\mathscr{DST}_{II}$, $\mathscr{DCT}_{II}$ and $\mathscr{DST}_{III}$. The shifting of indices is visualized in Fig. 4.

The inverse of the $\mathscr{DST}_{II}$ and $\mathscr{DCT}_{II}$ are the $\mathscr{DST}_{III}$ and $\mathscr{DCT}_{III}$, respectively. The $\mathscr{DST}_{III}$ is available from *FFTPACK* as subroutine *SINQ1F* and $\mathscr{DCT}_{III}$ as subroutine *COSQ1F*. Again, the k-values of the $\mathscr{DST}_{III}$ and $\mathscr{DCT}_{III}$ do not match. For computation of eq. (41), a function in Fourier space as result of a $\mathscr{DST}_{II}$ is transformed back to real space using the $\mathscr{DST}_{III}$ and $\mathscr{DCT}_{III}$. The $\mathscr{DST}_{III}$ can be performed immediately. For the inverse transform using the $\mathscr{DCT}_{III}$, the exact value $\widehat{f}_{k=0}^{\mathscr{DCT}} = 0$ has to be added. Therefore, $\widehat{f}_{k=N}^{\mathscr{DST}}$ is disregarded, which has negligible effect as $\widehat{f}_{k\to\infty}^{\mathscr{DCT}} \to 0$ for smooth functions and appropriate number of grid points. The shifting of indices is visualized in Fig. 5.

For computation of the appropriate discrete k-grid, the analytical sine transform can be discretized with $r_j = \left(j+\frac{1}{2}\right)\Delta z$ and $f(r_j) = f_j$. This leads to a similar equation as the discrete sine transform, eq. (71), according to

$$\begin{aligned} \widehat{f}(k_r) &= \int_{r=0}^{\infty} f(r)\sin(2\pi r k_r)\,\mathrm{d}r \\ &\approx \sum_{j=0}^{N-1} f_j \sin\left[2\pi\left(j+\frac{1}{2}\right)\Delta r k_r\right]\Delta r \end{aligned} \tag{73}$$

Comparison of the arguments of the sine functions in eqs. (72) and (73), $\frac{\pi}{N}\left(j+\frac{1}{2}\right)\left(k^*+1\right) = 2\pi\left(j+\frac{1}{2}\right)\Delta r k_r$ yields the discretization in Fourier space, according to

$$k_r = \frac{k^*+1}{2N\Delta z} = \frac{k^*+1}{2L_{\text{tot}}} \qquad \text{with } k^* = 0, \cdots, (N-1) \tag{74}$$

In contrast to eq. (53), we divide by $(2L_{\text{tot}})$, because the $\mathscr{DST}_{II}$ assumes odd continuation by considering only half of the domain compared to the corresponding Fourier transform. For N grid points, the k-vector for the computation of the discrete representation of the weight functions, eqs. (14) and (15), is

$$k_r^{\mathscr{DST}} = \frac{1}{2L_{\text{tot}}}[1, \cdots, N] \tag{75}$$

while the same approach leads to a k-vector for the $\mathscr{DCT}_{II}$, according to

$$k_r^{\mathscr{DCT}} = \frac{1}{2L_{\text{tot}}}[0, \cdots, (N-1)] \tag{76}$$

this yields a k_r-grid in Fourier space which is used for the analytical computation of the weight functions $\widehat{\omega}_i$, eqs. (14) and (15). These weight functions $\widehat{\omega}_i$ are then multiplied in Fourier space with the $\mathscr{DST}_{II}$ and $\mathscr{DCT}_{II}$ output of the function to be convolved, while this result can be directly transformed back to real space using the $\mathscr{DST}_{III}$ and $\mathscr{DCT}_{III}$ algorithms.

5. Performance analysis of FFT convolution

To compare the efficiency of convolution algorithms using fast Fourier or similar transforms (i.e. discrete sine, cosine and Abel transforms), we compare the performance of one-dimensional FFT convolutions, computed via

$$\rho \otimes \omega = \mathscr{F}_z^{-1}[\mathscr{F}_z[\rho(z)]\widehat{\omega}(k_z)] \tag{77}$$

with three real space convolution algorithms. We adapt the notation of the weighted densities defined in eq. (5).

The first real space convolution algorithm, hereafter referred to as *naïve* convolution, approximates the convolution integral of a density profile ρ with the weight function ω (each with N discretization points) over the whole discrete domain, where the value for the i-th element of the discrete sequence is computed according to Ref. [59].

$$(\rho \otimes \omega)_i = \frac{1}{N}\sum_{k=0}^{N-1} \omega_k \rho_{i-k} \qquad \forall i \tag{78}$$

The second real space algorithm, referred to as *compact* convolution, exploits the fact that weight functions are nonzero on a finite domain. As a consequence, the sequence for the weight function is shorter (length $M < N$) than the sequence for the density profile. Therefore, the value for the i-th element is computed as

$$(\rho \otimes \omega)_i = \frac{1}{M}\sum_{k=-\frac{M-1}{2}}^{\frac{M-1}{2}} \omega_k \rho_{i-k} \qquad \forall i \tag{79}$$

with the number of discretization points $M \in \{2n+1 \,|\, n \in \mathbb{N}^+\}$ for the weight function, which is always an odd number due to the symmetry of the weight function.

The third real space algorithm uses dense *matrix* multiplication

$$\rho \otimes \omega = \boldsymbol{\omega}\boldsymbol{\rho} \tag{80}$$

with the convolution matrix $\boldsymbol{\omega}$ and the density profile vector $\boldsymbol{\rho}$.

Fig. 6 depicts the computing time for one convolution using the

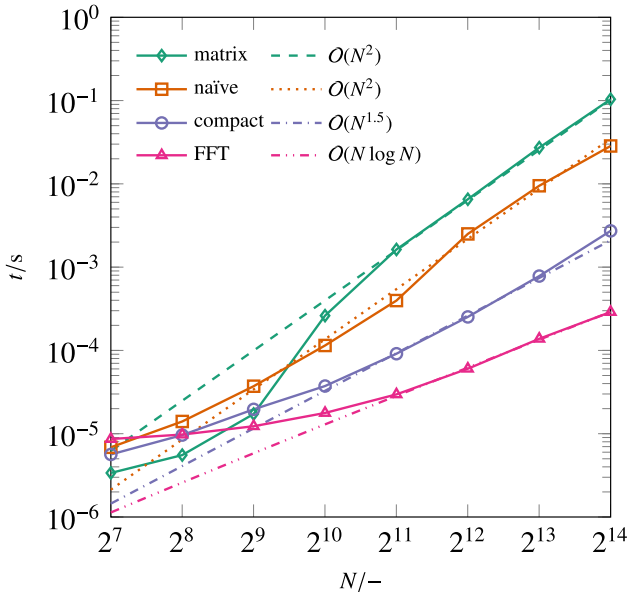

Fig. 6. Comparison of computing time t for one convolution using Fourier space, naïve, compact and matrix multiplication convolution, eqs. (77)–(80) respectively, for different number of grid points N, including scaling behavior $\mathscr{O}$. Length of the inner domain is $L_{\mathrm{in},z} = 100$ Å and the radius for convolution is $R = 1.8$ Å.

four algorithms defined in eqs. (77)–(80) with respect to the number of spatial discretization points N. Additionally, scaling behavior $\mathscr{O}$ of the used algorithms is presented (non-continuous lines).

For small system sizes N, convolutions with convolution matrices perform best, while computing times for naïve, compact and FFT convolutions are higher (staying in the same order of magnitude). For $N = 2^{14}$, the scaling behavior of the FFT, $\mathscr{O}(N\log N)$, renders the FFT convolution at least one order of magnitude faster than the remaining algorithms. For a large number of discretization points, convolutions using a matrix product, eq. (80), take the longest, while naïve convolutions, eq. (78), compute faster; both scaling with $\mathscr{O}(N^2)$. Compact convolutions, eq. (79), scale better with respect to approximately $\mathscr{O}(N^{1.5})$, making this convolution algorithm for large systems superior to the matrix product and naïve approach. FFT convolutions, eq. (77), scale best for large systems (here $N = 2^{14}$) according to $\mathscr{O}(N\log N)$, performing at least one order of magnitude better than the remaining algorithms. Even for typical number of discretization points $N = 2^{10} = 1024$ convolution algorithms exploiting fast Fourier or similar transforms perform best among the four considered numerical convolution approaches.

To summarize, convolution algorithms exploiting fast Fourier or similar transforms perform best for relevant systems among the four considered numerical convolution approaches.

6. Conclusion

This work serves as a guide on efficient numerical implementations of classical DFT methods in Cartesian, cylindrical and spherical coordinates using the convolution theorem of the Fourier transform. Applied to Helmholtz energy functionals expressed in terms of weighted densities, this allows for fast and easy DFT calculations using off-the-shelf algorithms: fast Fourier, Hankel, sine and cosine transforms. Especially for two- and three-dimensional problems, using Fourier space convolution simplifies computation of multi-dimensional convolution integrals compared to real space methods. The main text describes scalar-valued and vector-valued weighted densities that appear with FMT. The equations for a Helmholtz energy functional based on the perturbed-chain statistical associating fluid theory are explicitly written out in the Supporting Information.

Acknowledgments

The authors thank the German Research Foundation (DFG) for financial support through the collaborative research center *Droplet Dynamics Under Extreme Ambient Conditions* (SFB-TRR 75), the international research training group *Nonlinearities and Upscaling in Porous Media* (GRK 1398) and the collaborative research center *Interface-Driven Multi-Field Processes in Porous Media — Flow, Transport and Deformation* (SFB 1313, project number 327154368). We thank Thijs van Westen for his help improving this manuscript.

Appendix A. Fourier Transform for Calculation of Convolution Integrals

All convolution integrals occurring throughout this work are convolutions of either a functional derivative of the Helmholtz energy, or a density, with a suitable weight function ω. These convolution integrals can be calculated efficiently using fast Fourier transform algorithms. In this appendix, the Fourier transform $\mathscr{F}$ and its inverse $\mathscr{F}^{-1}$ in different coordinate systems are derived in pedagogical detail.

In Cartesian coordinates the standard fast Fourier transform can be used for all directions (for 1-D, 2-D and 3-D systems). For cylindrical coordinates, rotational symmetry (2-D) can be exploited, such that one can use the standard fast Fourier transform for the axial direction and the fast Hankel transform (of order 0 and 1 for scalar and vector weighted functions, respectively) for the radial direction. In cylindrical coordinates (1-D), only fast Hankel transforms are used. For spherically symmetric systems (1-D), fast sine/cosine transforms are used for the calculation of the Fourier and the inverse Fourier transform.

In the following, we lay out the details of how to compute the Fourier and inverse Fourier transform for Cartesian (1-D, 2-D & 3-D), cylindrical (2-D), cylindrical and spherical (1-D) coordinates. Detailed derivations are presented to show consistency of the approach and facilitate own implementations of DFT methods. The Fourier and inverse Fourier transform are defined as

$$\widehat{\mathfrak{f}}(\mathbf{k}) = \int \mathfrak{f}(\mathbf{r}) \mathrm{e}^{-2\pi \mathrm{i}\, \mathbf{r}\cdot\mathbf{k}}\, \mathrm{d}\mathbf{r} \tag{A.1}$$

$$\mathfrak{f}(\mathbf{r}) = \int \widehat{\mathfrak{f}}(\mathbf{k}) \mathrm{e}^{2\pi \mathrm{i}\, \mathbf{r}\cdot\mathbf{k}}\, \mathrm{d}\mathbf{k} \tag{A.2}$$

with $\mathfrak{f}$ as the function to be transformed, the imaginary unit i, and the position vector in real and Fourier space $\mathbf{r}$ and $\mathbf{k}$, respectively. Here, $\mathbf{r}\cdot\mathbf{k}$ stands for the dot product of two vectors, and the circumflex $\widehat{\ }$ indicates the function being considered in Fourier space. By exploiting symmetry in the appropriate coordinate system, the Fourier transform from eq. (A.1) can be used for the derivation of the appropriate integral transform. In the following, integral transforms for Cartesian, cylindrical and spherical coordinates are calculated for scalar and vector-valued functions $\mathfrak{f} = \{f, \mathbf{f}\}$, respectively.

A.1. Cartesian Coordinates

The Fourier transform is formulated in Cartesian coordinates,

therefore, the Cartesian vectors are used for the dot product of **r** and **k**, leading to

$$\mathbf{r}\cdot\mathbf{k}=\begin{pmatrix}x\\y\\z\end{pmatrix}\cdot\begin{pmatrix}k_x\\k_y\\k_z\end{pmatrix}=xk_x+yk_y+zk_z \tag{A.3}$$

and the volume integral in eq. (A.1) simplifies to a triple integral with volume element $\mathrm{d}\mathbf{r}=\mathrm{d}x\,\mathrm{d}y\,\mathrm{d}z$, leading to

$$\begin{aligned}\hat{\mathfrak{f}}(k_x,k_y,k_z) &= \int_{z=-\infty}^{\infty}\int_{y=-\infty}^{\infty}\int_{x=-\infty}^{\infty}\mathfrak{f}(x,y,z)\mathrm{e}^{-2\pi\mathrm{i}\,xk_x}\,\mathrm{d}x\\ &\quad\times\mathrm{e}^{-2\pi\mathrm{i}\,yk_y}\,\mathrm{d}y\,\mathrm{e}^{-2\pi\mathrm{i}\,zk_z}\,\mathrm{d}z\\ &= \mathscr{F}_x\mathscr{F}_y\mathscr{F}_z[\mathfrak{f}(x,y,z)]\end{aligned} \tag{A.4}$$

The inverse Fourier transform is computed similarly, according to

$$\begin{aligned}\mathfrak{f}(x,y,z) &= \int_{k_z=-\infty}^{\infty}\int_{k_y=-\infty}^{\infty}\int_{k_x=-\infty}^{\infty}\hat{\mathfrak{f}}(k_x,k_y,k_z)\mathrm{e}^{2\pi\mathrm{i}\,xk_x}\,\mathrm{d}k_x\\ &\quad\times\mathrm{e}^{2\pi\mathrm{i}\,yk_y}\,\mathrm{d}k_y\,\mathrm{e}^{2\pi\mathrm{i}\,zk_z}\,\mathrm{d}k_z\\ &= \mathscr{F}_x^{-1}\mathscr{F}_y^{-1}\mathscr{F}_z^{-1}\left[\hat{\mathfrak{f}}(k_x,k_y,k_z)\right]\end{aligned} \tag{A.5}$$

A.1.1. Fourier Transform of Scalar Quantities

The *x*-, *y*- and *z*-direction of the Fourier transform can be separated according to

$$\hat{f}(k_x,k_y,k_z)=\mathscr{F}_x\mathscr{F}_y\mathscr{F}_z[f(x,y,z)] \tag{A.6}$$

Yielding a Fourier transform in each direction.

A.1.2. Inverse Fourier Transform of Scalar Quantities

The inverse transform can be treated analogously, leading to

$$f(x,y,z)=\mathscr{F}_x^{-1}\mathscr{F}_y^{-1}\mathscr{F}_z^{-1}\left[\hat{f}(k_x,k_y,k_z)\right] \tag{A.7}$$

A.1.3. Fourier Transform of Vector Quantities

The Fourier transform of vector quantities is performed by splitting the vector into its different contributions depending on the underlying coordinate system. For the case of Cartesian unit vectors.

$$\mathbf{e}_x=\begin{pmatrix}1\\0\\0\end{pmatrix},\mathbf{e}_y=\begin{pmatrix}0\\1\\0\end{pmatrix},\mathbf{e}_z=\begin{pmatrix}0\\0\\1\end{pmatrix} \tag{A.8}$$

The vector-valued function **f** can be represented according to

$$\mathbf{f}(x,y,z)=\begin{pmatrix}f_x\\f_y\\f_z\end{pmatrix}=f_x\mathbf{e}_x+f_y\mathbf{e}_y+f_z\mathbf{e}_z \tag{A.9}$$

Although this detailed treatment may not be necessary here, we include it nonetheless, as it will help to understand the forthcoming treatment in cylindrical and spherical coordinates. The Fourier transform of **f** is calculated via

$$\begin{aligned}\hat{\mathbf{f}}(k_x,k_y,k_z) &= \int_{z=-\infty}^{\infty}\int_{y=-\infty}^{\infty}\int_{x=-\infty}^{\infty}\begin{pmatrix}f_x(x,y,z)\\f_y(x,y,z)\\f_z(x,y,z)\end{pmatrix}\\ &\quad\times\mathrm{e}^{-2\pi\mathrm{i}\,xk_x}\,\mathrm{d}x\,\mathrm{e}^{-2\pi\mathrm{i}\,yk_y}\,\mathrm{d}y\,\mathrm{e}^{-2\pi\mathrm{i}\,zk_z}\,\mathrm{d}z\end{aligned} \tag{A.10}$$

Or element-wise, as

$$\hat{\mathbf{f}}(k_x,k_y,k_z)=\begin{pmatrix}\hat{f}_{k_x}(k_x,k_y,k_z)\\\hat{f}_{k_y}(k_x,k_y,k_z)\\\hat{f}_{k_z}(k_x,k_y,k_z)\end{pmatrix}=\begin{pmatrix}\mathscr{F}_x\mathscr{F}_y\mathscr{F}_z[f_x(x,y,z)]\\\mathscr{F}_x\mathscr{F}_y\mathscr{F}_z[f_y(x,y,z)]\\\mathscr{F}_x\mathscr{F}_y\mathscr{F}_z[f_z(x,y,z)]\end{pmatrix} \tag{A.11}$$

Each of the elements of the vector-valued function can be transformed to Fourier space individually and, just as for scalar-valued functions, can be transformed for every direction separately.

A.1.4. Inverse Fourier Transform of Vector Quantities

Treatment of the inverse transform of a vector quantity is analogous to the treatment laid out in the previous section, i.e. with the Cartesian unit vectors in Fourier space

$$\mathbf{e}_{k_x}=\begin{pmatrix}1\\0\\0\end{pmatrix},\mathbf{e}_{k_y}=\begin{pmatrix}0\\1\\0\end{pmatrix},\mathbf{e}_{k_z}=\begin{pmatrix}0\\0\\1\end{pmatrix} \tag{A.12}$$

the vector-valued function $\hat{\mathbf{f}}$ can be represented according to

$$\hat{\mathbf{f}}(k_x,k_y,k_z)=\begin{pmatrix}\hat{f}_{k_x}\\\hat{f}_{k_y}\\\hat{f}_{k_z}\end{pmatrix}=\hat{f}_{k_x}\mathbf{e}_{k_x}+\hat{f}_{k_y}\mathbf{e}_{k_y}+\hat{f}_{k_z}\mathbf{e}_{k_z} \tag{A.13}$$

The inverse Fourier transform of $\hat{\mathbf{f}}$ is calculated as

$$\begin{aligned}\mathbf{f}(x,y,z) &= \int_{k_z=-\infty}^{\infty}\int_{k_y=-\infty}^{\infty}\int_{k_x=-\infty}^{\infty}\begin{pmatrix}\hat{f}_{k_x}(k_x,k_y,k_z)\\\hat{f}_{k_y}(k_x,k_y,k_z)\\\hat{f}_{k_z}(k_x,k_y,k_z)\end{pmatrix}\\ &\quad\times\mathrm{e}^{2\pi\mathrm{i}\,xk_x}\,\mathrm{d}k_x\,\mathrm{e}^{2\pi\mathrm{i}\,yk_y}\,\mathrm{d}k_y\,\mathrm{e}^{2\pi\mathrm{i}\,zk_z}\,\mathrm{d}k_z\\ &= \begin{pmatrix}f_x(x,y,z)\\f_y(x,y,z)\\f_z(,y,z)\end{pmatrix}\\ &= \begin{pmatrix}\mathscr{F}_x^{-1}\mathscr{F}_y^{-1}\mathscr{F}_z^{-1}\left[\hat{f}_{k_x}(k_x,k_y,k_z)\right]\\\mathscr{F}_x^{-1}\mathscr{F}_y^{-1}\mathscr{F}_z^{-1}\left[\hat{f}_{k_y}(k_x,k_y,k_z)\right]\\\mathscr{F}_x^{-1}\mathscr{F}_y^{-1}\mathscr{F}_z^{-1}\left[\hat{f}_{k_z}(k_x,k_y,k_z)\right]\end{pmatrix}\end{aligned} \tag{A.14}$$

Each of the elements of the vector-valued function can be transformed to Fourier space individually and, just as for scalar-valued functions, can be transformed for every direction consecutively.

A.1.5. Treatment of 1-D & 2-D Cartesian Coordinates

Fourier transform of 1-D or 2-D Cartesian coordinates can be understood as a subset of the 3-D Fourier transform. The dot product in eq. (A.3) for one dimension in *x*-direction is $\mathbf{r}\cdot\mathbf{k}=xk_x$. This simplifies the Fourier, eq. (A.4), and inverse Fourier transform, eq. (A.5), to $\hat{\mathfrak{f}}(k_x)=\mathscr{F}_x[\mathfrak{f}(x)]$ and $\mathfrak{f}(x)=\mathscr{F}_x^{-1}[\hat{\mathfrak{f}}(k_x)]$, respectively. The Fourier and its inverse transform of a scalar quantity result in

$$\widehat{f}(k_x) = \mathscr{F}_x[f(x)] \tag{A.15}$$

$$f(x) = \mathscr{F}_x^{-1}\left[\widehat{f}(k_x)\right] \tag{A.16}$$

For a vector quantity, the Fourier and its inverse transform yield

$$\widehat{\mathbf{f}}(k_x) = \mathscr{F}_x[f_x(x)] \tag{A.17}$$

$$\mathbf{f}(x) = \mathscr{F}_x^{-1}\left[\widehat{f}_{k_x}(k_x)\right] \tag{A.18}$$

2-D Cartesian coordinates are the consequence of disregarding one dimension from the general 3-D case.

A.2. Cylindrical Coordinates

In cylindrical coordinates, the dot product $\mathbf{r}\cdot\mathbf{k}$ is calculated as

$$r\cdot k = \begin{pmatrix} r\cos\phi \\ r\sin\phi \\ z \end{pmatrix} \cdot \begin{pmatrix} k_r\cos k_\phi \\ k_r\sin k_\phi \\ k_z \end{pmatrix} \tag{A.19}$$

with the radial coordinate r and k_r in the polar plane, the azimuthal angle ϕ and k_ϕ, and the axial direction z and k_z, in real and Fourier space, respectively. The identity $\cos\phi\cos k_\phi + \sin\phi\sin k_\phi = \cos(\phi - k_\phi) = \cos(k_\phi - \phi)$ simplifies eq. (A.19) to

$$\mathbf{r}\cdot\mathbf{k} = rk_r\cos\phi + zk_z \tag{A.20}$$

where we chose a $\mathbf{k}$-vector parallel to the k_x-axis in Fourier space which implies $k_\phi = 0$. With the volume element $\mathrm{d}\mathbf{r} = r\,\mathrm{d}\phi\,\mathrm{d}r\,\mathrm{d}z$, and the result of eq. (A.20), the Fourier transform from eq. (A.1) can be written as

$$\widehat{\mathfrak{f}}(k_r, k_z) = \int_{z=-\infty}^{\infty}\int_{r=0}^{\infty}\mathfrak{f}(r,z)\int_{\phi=0}^{2\pi} \mathrm{e}^{-2\pi\mathrm{i}\,rk_r\cos\phi}\,\mathrm{d}\phi\,r\;\mathrm{d}r\,\mathrm{e}^{-2\pi\mathrm{i}\,zk_z}\,\mathrm{d}z \tag{A.21}$$

The inverse Fourier transform can be computed analogously, leading to

$$\mathfrak{f}(r,z) = \int_{k_z=-\infty}^{\infty}\int_{k_r=0}^{\infty}\widehat{\mathfrak{f}}(k_r,k_z)\int_{k_\phi=0}^{2\pi} \mathrm{e}^{2\pi\mathrm{i}\,rk_r\cos k_\phi}\,\mathrm{d}k_\phi\,k_r\;\mathrm{d}k_r\,\mathrm{e}^{2\pi\mathrm{i}\,zk_z}\,\mathrm{d}k_z \tag{A.22}$$

A.2.1. Cylindrical Fourier Transform of Scalar Quantities

We consider cases of rotational symmetry, where the integral in eq. (A.21) simplifies through integration. With the definition of the Bessel function of first kind and zeroth order

$$\mathrm{J}_0(\xi) = \frac{1}{2\pi}\int_{\phi=0}^{2\pi}\mathrm{e}^{\mathrm{i}\,\xi\cos\phi}\,\mathrm{d}\phi \tag{A.23}$$

with dummy variable ξ and the identity $\mathrm{J}_0(-\xi) = \mathrm{J}_0(\xi)$, the Fourier transform from eq. (A.1) simplifies to

$$\widehat{f}(k_r,k_z) = \int_{z=-\infty}^{\infty} 2\pi \int_{r=0}^{\infty} f(r,z) r\mathrm{J}_0(2\pi r k_r)\,\mathrm{d}r\,\mathrm{e}^{-2\pi\mathrm{i}\,zk_z}\,\mathrm{d}z \tag{A.24}$$

The integration over the r-coordinate can be performed using the Hankel transform $\mathscr{H}$, which for order ν is defined as

$$\mathscr{H}_\nu[f(r)] = 2\pi\int_0^\infty f(r) r\mathrm{J}_\nu(2\pi r k_r)\,\mathrm{d}r \tag{A.25}$$

With the Bessel function of first kind and ν-th order J_ν. Performing the integration over z using the Fourier transform $\mathscr{F}_z$, the Fourier transform of $f(r,z)$ follows as

$$\widehat{f}(k_r,k_z) = \mathscr{F}_z\mathscr{H}_0[f(r,z)] \tag{A.26}$$

A.2.2. Cylindrical Inverse Fourier Transform of Scalar Quantities

Because the Bessel function of first kind and zeroth order is even $\mathrm{J}_0(\xi) = \mathrm{J}_0(-\xi)$, the inverse Fourier transform $\widehat{f}(k_r,k_z)$ can be computed analogous to the previous section as

$$f(r,z) = \mathscr{F}_z^{-1}\mathscr{H}_0^{-1}\left[\widehat{f}(k_r,k_z)\right] \tag{A.27}$$

with the inverse Hankel transform $\mathscr{H}_\nu^{-1}$ of order ν of the k_r-coordinate as

$$\mathscr{H}_\nu^{-1}\left[\widehat{f}(k_r)\right] = 2\pi\int_0^\infty \widehat{f}(k_r) k_r \mathrm{J}_\nu(2\pi r k_r)\,\mathrm{d}k_r \tag{A.28}$$

and the inverse Fourier transform $\mathscr{F}_z^{-1}$ of the k_z-coordinate.

A.2.3. Cylindrical Fourier Transform of Vector Quantities

Analogous to Appendix A.1.3, the Fourier transform of vector quantities in cylindrical coordinates is performed by splitting the vector into its different contributions: radial f_r, azimuthal f_ϕ and axial f_z, with their respective unit vectors, according to

$$\mathbf{e}_r = \begin{pmatrix}\cos\phi\\ \sin\phi\\ 0\end{pmatrix}, \mathbf{e}_\phi = \begin{pmatrix}-\sin\phi\\ \cos\phi\\ 0\end{pmatrix}, \mathbf{e}_z = \begin{pmatrix}0\\0\\1\end{pmatrix} \tag{A.29}$$

These unit vectors are defined in a Cartesian frame of reference, which allows the Fourier transforms to be treated analogously to the above regarded case in Cartesian coordinates. The vector quantity can then be decomposed into three parts, as

$$\mathbf{f}(r,\phi,z) = f_r\mathbf{e}_r + f_\phi\mathbf{e}_\phi + f_z\mathbf{e}_z \tag{A.30}$$

However, due to rotational symmetry $\mathbf{f}$ is only a function of the radius r and the axial coordinate z, whereas the azimuthal contribution equals zero, $f_\phi = 0$, leading to

$$\mathbf{f}(r,\phi,z) = f_r\begin{pmatrix}\cos\phi\\ \sin\phi\\ 0\end{pmatrix} + f_z\begin{pmatrix}0\\0\\1\end{pmatrix} \tag{A.31}$$

The Fourier transform of $\mathbf{f}$ is then calculated as

$$\widehat{\mathbf{f}}(k_r,k_z) = \int_{z=-\infty}^{\infty}\int_{r=0}^{\infty}\int_{\varphi=0}^{2\pi}\begin{pmatrix}f_r(r,z)\cos\varphi\\ f_r(r,z)\sin\varphi\\ f_z(r,z)\end{pmatrix} \times\mathrm{e}^{-2\pi\mathrm{i}\,rk_r\cos\varphi}\,\mathrm{d}\varphi\;r\;\mathrm{d}r\,\mathrm{e}^{-2\pi\mathrm{i}\,zk_z}\,\mathrm{d}z \tag{A.32}$$

With the definition of Bessel's first integral of order ν for Bessel

functions of first kind

$$\mathrm{J}_\nu(\xi) = \frac{1}{2\pi \mathrm{i}^{\,\nu}} \int_{\phi=0}^{2\pi} \mathrm{e}^{\mathrm{i}\,\xi\,\cos\,\phi}\,\cos(\nu\phi)\,\mathrm{d}\phi \tag{A.33}$$

eq. (A.32) simplifies to

$$\begin{aligned}\widehat{\mathbf{f}}(k_r,k_z) &= \int_{z=-\infty}^{\infty} 2\pi \int_{r=0}^{\infty} \begin{pmatrix} -\mathrm{i}\,f_r(r,z)\mathrm{J}_1(2\pi r k_r) \\ 0 \\ f_z(r,z)\mathrm{J}_0(2\pi r k_r) \end{pmatrix} \\ &\quad \times r\;\mathrm{d}r\,\mathrm{e}^{-2\pi\mathrm{i}\,zk_z}\,\mathrm{d}z\end{aligned} \tag{A.34}$$

after utilization of $\mathrm{J}_0(-\xi) = \mathrm{J}_0(\xi)$ and $\mathrm{J}_1(-\xi) = -\,\mathrm{J}_1(\xi)$. Finally, the Hankel transform, eq. (A.25), and the Fourier transform can be exploited, leading to

$$\begin{aligned}\widehat{\mathbf{f}}(k_r,k_z) &= \int_{z=-\infty}^{\infty} \begin{pmatrix} \mathscr{H}_1[-\mathrm{i}\,f_r(r,z)] \\ 0 \\ \mathscr{H}_0[f_z(r,z)] \end{pmatrix} \mathrm{e}^{-2\pi\mathrm{i}\,zk_z}\,\mathrm{d}z \\ &= \begin{pmatrix} \mathscr{F}_z\mathscr{H}_1[-\mathrm{i}\,f_r(r,z)] \\ 0 \\ \mathscr{F}_z\mathscr{H}_0[f_z(r,z)] \end{pmatrix}\end{aligned} \tag{A.35}$$

A.2.4. Cylindrical Inverse Fourier Transform of Vector Quantities

Treatment of the inverse transform of a vector quantity is analogous to the treatment laid out in the previous section, i.e. with the unit vectors in cylindrical coordinates in Fourier space

$$\mathbf{e}_{k_r} = \begin{pmatrix} \cos k_\phi \\ \sin k_\phi \\ 0 \end{pmatrix}, \mathbf{e}_{k_\phi} = \begin{pmatrix} -\sin k_\phi \\ \cos k_\phi \\ 0 \end{pmatrix}, \mathbf{e}_{k_z} = \begin{pmatrix} 0 \\ 0 \\ 1 \end{pmatrix} \tag{A.36}$$

The vector-valued function $\widehat{\mathbf{f}}$ can be represented according to

$$\widehat{\mathbf{f}}(k_r,k_\phi,k_z) = \widehat{f}_{k_r}\mathbf{e}_{k_r} + \widehat{f}_{k_\phi}\mathbf{e}_{k_\phi} + \widehat{f}_{k_z}\mathbf{e}_{k_z} \tag{A.37}$$

Due to rotational symmetry $\widehat{\mathbf{f}}$ is only a function of the radius k_r and the axial coordinate k_z (the azimuthal contribution equals zero, $\widehat{f}_{k_\phi} = 0$), this leads to

$$\widehat{\mathbf{f}}(k_r,k_\phi,k_z) = \widehat{f}_{k_r}\begin{pmatrix} \cos k_\phi \\ \sin k_\phi \\ 0 \end{pmatrix} + \widehat{f}_{k_z}\begin{pmatrix} 0 \\ 0 \\ 1 \end{pmatrix} \tag{A.38}$$

Applying the inverse Fourier transform yields

$$\begin{aligned}\mathbf{f}(r,z) &= \int_{k_z=-\infty}^{\infty}\int_{k_r=0}^{\infty}\int_{k_\phi=0}^{2\pi} \begin{pmatrix} \widehat{f}_{k_r}(k_r,k_z)\cos k_\phi \\ \widehat{f}_{k_r}(k_r,k_z)\sin k_\phi \\ \widehat{f}_{k_z}(k_r,k_z) \end{pmatrix} \\ &\quad \times \mathrm{e}^{2\pi\mathrm{i}\,rk_r\cos k_\varphi}\,\mathrm{d}k_\varphi\;k_r\;\mathrm{d}k_r\mathrm{e}^{2\pi\mathrm{i}\,zk_z}\,\mathrm{d}k_z\end{aligned} \tag{A.39}$$

With the definition of Bessel's first integral of order ν for Bessel functions of first kind and zeroth J_0 and first order J_1.

$$\mathrm{J}_\nu(\xi) = \frac{1}{2\pi \mathrm{i}^{\,\nu}} \int_{k_\phi=0}^{2\pi} \mathrm{e}^{\mathrm{i}\,\xi\cos(k_\phi)}\,\cos(\nu k_\phi)\,\mathrm{d}k_\phi \tag{A.40}$$

eq. (A.39) simplifies to

$$\begin{aligned}\mathbf{f}(r,z) &= \int_{k_z=-\infty}^{\infty} 2\pi \int_{k_r=0}^{\infty} \begin{pmatrix} \mathrm{i}\,\widehat{f}_{k_r}(k_r,k_z)\mathrm{J}_1(2\pi r k_r) \\ 0 \\ \widehat{f}_{k_z}(k_r,k_z)\mathrm{J}_0(2\pi r k_r) \end{pmatrix} \\ &\quad \times k_r\;\mathrm{d}k_r\,\mathrm{e}^{2\pi\mathrm{i}\,zk_z}\,\mathrm{d}k_z\end{aligned} \tag{A.41}$$

Finally, the Hankel transform, eq. (A.25), and the inverse Fourier transform can be exploited, leading to

$$\begin{aligned}\mathbf{f}(r,z) &= \int_{k_z=-\infty}^{\infty} \begin{pmatrix} \mathscr{H}_1^{-1}[\mathrm{i}\,\widehat{f}_{k_r}(k_r,k_z)] \\ 0 \\ \mathscr{H}_0^{-1}[\widehat{f}_{k_z}(k_r,k_z)] \end{pmatrix} \mathrm{e}^{2\pi\mathrm{i}\,zk_z}\,\mathrm{d}k_z \\ &= \begin{pmatrix} \mathscr{F}_z^{-1}\mathscr{H}_1^{-1}[\mathrm{i}\,\widehat{f}_{k_r}(k_r,k_z)] \\ 0 \\ \mathscr{F}_z^{-1}\mathscr{H}_0^{-1}[\widehat{f}_{k_z}(k_r,k_z)] \end{pmatrix}\end{aligned} \tag{A.42}$$

Note the different sign in the radial component compared to eq. (A.35), this is due to J_1 being an odd function.

A.2.5. Treatment of 1-D Cylindrical Coordinates

Fourier transform of one dimension in cylindrical coordinates can be understood as a subset of the two dimensional Fourier transform in cylindrical coordinates. The dot product in eq. (A.20) simplifies for one dimension to $\mathbf{r}\cdot\mathbf{k} = rk_r\cos\phi$. This simplifies the Fourier, eq. (A.21), and inverse Fourier transform, eq. (A.22). The Fourier and its inverse transform of a scalar quantity result in

$$\widehat{f}(k_r) = \mathscr{H}_0[f(r)] \tag{A.43}$$

$$f(r) = \mathscr{H}_0^{-1}[\widehat{f}(k_r)] \tag{A.44}$$

For a vector quantity, the Fourier and its inverse transform yield

$$\widehat{\mathbf{f}}(k_r) = \mathscr{H}_1[-\mathrm{i}\,f_r(r)] \tag{A.45}$$

$$\mathbf{f}(r) = \mathscr{H}_1^{-1}[\mathrm{i}\,\widehat{f}_{k_r}(k_r)] \tag{A.46}$$

A.3. Spherical Coordinates

For spherical coordinates, $\mathbf{r}\cdot\mathbf{k}$ can be written as

$$\mathbf{r}\cdot\mathbf{k} = \begin{pmatrix} r\cos\phi\sin\vartheta \\ r\sin\phi\sin\vartheta \\ r\cos\vartheta \end{pmatrix} \cdot \begin{pmatrix} k_r\cos k_\phi\sin k_\vartheta \\ k_r\sin k_\phi\sin k_\vartheta \\ k_r\cos k_\vartheta \end{pmatrix} \tag{A.47}$$

with radial coordinate r and k_r, azimuthal angle ϕ and k_ϕ, and polar angle ϑ and k_ϑ, in real and Fourier space, respectively. We limit consideration to cases of rotational symmetry. Spherical symmetry can be exploited utilizing the identity $\cos\vartheta\cos k_\vartheta + \sin\vartheta\sin k_\vartheta = \cos(\vartheta - k_\vartheta) = \cos(k_\vartheta - \vartheta)$ and choosing a $\mathbf{k}$-vector parallel to the k_z-axis in Fourier space with $\mathbf{k} = (0,0,k)^\top$ which implies $k_\vartheta = 0$. This simplifies the dot product $\mathbf{r}\cdot\mathbf{k}$ in eq. (A.47) to

$$\mathbf{r}\cdot\mathbf{k} = rk_r\cos\vartheta \tag{A.48}$$

With the volume element $\mathrm{d}\mathbf{r} = r^2\sin\vartheta\,\mathrm{d}\phi\,\mathrm{d}\vartheta\,\mathrm{d}r$, and the result of eq. (A.48), the Fourier transform, eq. (A.1), is calculated according to

$$\widehat{\mathfrak{f}}(k_r) = \int_{r=0}^{\infty}\int_{\vartheta=0}^{\pi}\int_{\phi=0}^{2\pi} \mathfrak{f}(r)\mathrm{e}^{-2\pi\mathrm{i}\,rk_r\cos\vartheta} r^2\sin\vartheta\,\mathrm{d}\phi\,\mathrm{d}\vartheta\,\mathrm{d}r \tag{A.49}$$

The inverse Fourier transform can be computed analogously, as

$$\check{\mathrm{f}}(r) = \int_{k_r=0}^{\infty}\int_{k_\vartheta=0}^{\pi}\int_{k_\phi=0}^{2\pi} \widehat{\mathrm{f}}(k_r)\mathrm{e}^{2\pi\mathrm{i}\,rk_r\cos k_\vartheta}k_r^2\sin k_\vartheta\,\mathrm{d}k_\phi\,\mathrm{d}k_\vartheta\,\mathrm{d}k_r \tag{A.50}$$

A.3.1. Spherical Fourier Transform of Scalar Quantities

Due to spherical symmetry, the integral in eq. (A.49) simplifies through integration. Integration over ϕ yields $\int_0^{2\pi}\mathrm{d}\phi = 2\pi$. Via substitution we can integrate over ϑ with $u = \cos\vartheta$ and $\mathrm{d}u = -\sin\vartheta\,\mathrm{d}\vartheta$, leading to

$$\begin{aligned}\widehat{f}(k_r) &= -2\pi\int_{r=0}^{\infty}\int_{u=1}^{-1} f(r)\mathrm{e}^{-2\pi\mathrm{i}\,rk_r u}r^2\,\mathrm{d}u\,\mathrm{d}r \\ &= \int_{r=0}^{\infty} f(r)\frac{\mathrm{e}^{2\pi\mathrm{i}\,rk_r}-\mathrm{e}^{-2\pi\mathrm{i}\,rk_r}}{\mathrm{i}\,rk_r}r^2\,\mathrm{d}r\end{aligned} \tag{A.51}$$

Using Euler's formula yields

$$\widehat{f}(k_r) = \frac{2}{k_r}\int_{r=0}^{\infty} f(r)r\sin(2\pi rk_r)\,\mathrm{d}r \equiv \frac{2}{k_r}\mathscr{SIN}[f(r)r] \tag{A.52}$$

with the definition of the sine transform $\mathscr{SIN}$. The Fourier transform for spherically symmetric systems simplifies to the sine transform.

A.3.2. Spherical Inverse Fourier Transform of Scalar Quantities

Treatment of the inverse transform, eq. (A.50), is analogous to the treatment laid out in the previous section, i.e.

$$f(r) = \frac{2}{r}\int_{k_r=0}^{\infty}\widehat{f}(k_r)k_r\sin(2\pi rk_r)\,\mathrm{d}k_r \equiv \frac{2}{r}\mathscr{SIN}[\widehat{f}(k_r)k_r] \tag{A.53}$$

with the self-inverse sine transform $\mathscr{SIN}$.

A.3.3. Spherical Fourier Transform of Vector Quantities

Analogous to Appendices A.1.3 and A.2.3, the Fourier transform of vector quantities in spherical coordinates is performed by separating the vector into different contributions: radial f_r, polar f_ϑ, and azimuthal f_ϕ, with their respective unit vectors, according to

$$\mathbf{e}_r = \begin{pmatrix}\cos\phi\sin\vartheta\\ \sin\phi\sin\vartheta\\ \cos\vartheta\end{pmatrix}, \mathbf{e}_\vartheta = \begin{pmatrix}\cos\phi\cos\vartheta\\ \sin\phi\cos\vartheta\\ -\sin\vartheta\end{pmatrix}, \mathbf{e}_\phi = \begin{pmatrix}-\sin\phi\\ \cos\phi\\ 0\end{pmatrix} \tag{A.54}$$

$$\mathbf{f}(r,\vartheta,\phi) = f_r\mathbf{e}_r + f_\vartheta\mathbf{e}_\vartheta + f_\phi\mathbf{e}_\phi \tag{A.55}$$

However, due to spherical symmetry $\mathbf{f}$ is only a function of the radius $r = |\mathbf{r}|$. Therefore, both other contributions equal zero, $f_\vartheta = 0 = f_\phi$, leading to

$$\mathbf{f}(r,\vartheta,\phi) = f_r\begin{pmatrix}\cos\phi\sin\vartheta\\ \sin\phi\sin\vartheta\\ \cos\vartheta\end{pmatrix} \tag{A.56}$$

The Fourier transform of $\mathbf{f}$ then yields

$$\begin{aligned}\widehat{\mathbf{f}}(k_r) = &\int_{r=0}^{\infty}\int_{\vartheta=0}^{\pi}\int_{\phi=0}^{2\pi}\begin{pmatrix}f_r(r)\cos\phi\sin\vartheta\\ f_r(r)\sin\phi\sin\vartheta\\ f_r(r)\cos\vartheta\end{pmatrix} \\ &\times\mathrm{e}^{-2\pi\mathrm{i}\,rk_r\cos\vartheta}r^2\sin\vartheta\,\mathrm{d}\phi\,\mathrm{d}\vartheta\,\mathrm{d}r\end{aligned} \tag{A.57}$$

Performing the integration over ϕ leads to vanishing contributions for the first and second vector entry due to $\int_{\phi=0}^{2\pi}\cos(\phi)\,\mathrm{d}\phi = 0$ and $\int_{\phi=0}^{2\pi}\sin(\phi)\,\mathrm{d}\phi = 0$. As a result, we only regard the z-direction, leading to

$$\widehat{\mathbf{f}}(k_r) = \int_{r=0}^{\infty}\int_{\vartheta=0}^{\pi} f_r(r)\begin{pmatrix}0\\ 0\\ 2\pi\cos\vartheta\end{pmatrix}\mathrm{e}^{-2\pi\mathrm{i}\,rk_r\cos\vartheta}r^2\sin\vartheta\,\mathrm{d}\vartheta\,\mathrm{d}r \tag{A.58}$$

With $(0,0,2\pi\cos(\vartheta))^\top = 2\pi\cos(\vartheta)\mathbf{e}_z$, eq. (A.58) yields

$$\widehat{\mathbf{f}}(k_r) = \mathbf{e}_z\int_{r=0}^{\infty}\int_{\vartheta=0}^{\pi} f_r(r)2\pi\cos\vartheta\,\mathrm{e}^{-2\pi\mathrm{i}\,rk_r\cos\vartheta}r^2\sin\vartheta\,\mathrm{d}\vartheta\,\mathrm{d}r \tag{A.59}$$

Integration over ϑ is carried out using the substitution $u = \cos\vartheta$ and $\mathrm{d}u = -\sin\vartheta\,\mathrm{d}\vartheta$ followed by partial integration, leading to

$$\begin{aligned}\widehat{\mathbf{f}}(k_r) &= -\mathbf{e}_z\int_{r=0}^{\infty}\int_{u=1}^{-1} f_r(r)2\pi u\mathrm{e}^{-2\pi\mathrm{i}\,rk_r u}r^2\,\mathrm{d}u\,\mathrm{d}r \\ &= -\mathbf{e}_z\int_{r=0}^{\infty} f_r(r)\left(\frac{\mathrm{e}^{2\pi\mathrm{i}\,rk_r}+\mathrm{e}^{-2\pi\mathrm{i}\,rk_r}}{\mathrm{i}\,rk_r} + \frac{\mathrm{e}^{-2\pi\mathrm{i}\,rk_r}-\mathrm{e}^{2\pi\mathrm{i}\,rk_r}}{2\pi(\mathrm{i}\,rk_r)^2}\right)r^2\,\mathrm{d}r\end{aligned} \tag{A.60}$$

Using Euler's formula gives

$$\begin{aligned}\widehat{\mathbf{f}}(k_r) = &\ \mathbf{e}_z\frac{2\mathrm{i}}{k_r}\int_{r=0}^{\infty} f_r(r)r\cos(2\pi rk_r)\,\mathrm{d}r \\ &-\mathbf{e}_z\frac{\mathrm{i}}{\pi k_r^2}\int_{r=0}^{\infty} f_r(r)\sin(2\pi rk_r)\,\mathrm{d}r\end{aligned} \tag{A.61}$$

Due to alignment of vector $\mathbf{k}$ in Fourier space with $\mathbf{e}_z$, implying $\mathbf{e}_z = \mathbf{e}_{k_r}$ we obtain a combination of sine ($\mathscr{SIN}$) and cosine transform ($\mathscr{COS}$), according to

$$\widehat{\mathbf{f}}(k_r) = \mathbf{e}_{k_r}\frac{2\mathrm{i}}{k_r}\mathscr{COS}[f_r(r)r] - \mathbf{e}_{k_r}\frac{\mathrm{i}}{\pi k_r^2}\mathscr{SIN}[f_r(r)] \tag{A.62}$$

A.3.4. Spherical Inverse Fourier Transform of Vector Quantities

Treatment of the inverse transform of a vector quantity is similar to the treatment in the previous section, i.e. with the unit vectors in spherical coordinates in Fourier space

$$\mathbf{e}_{k_r} = \begin{pmatrix}\cos k_\phi\sin k_\vartheta\\ \sin k_\phi\sin k_\vartheta\\ \cos k_\vartheta\end{pmatrix}, \mathbf{e}_{k_\vartheta} = \begin{pmatrix}\cos k_\phi\cos k_\vartheta\\ \sin k_\phi\cos k_\vartheta\\ -\sin k_\vartheta\end{pmatrix}, \mathbf{e}_{k_\phi} = \begin{pmatrix}-\sin k_\phi\\ \cos k_\phi\\ 0\end{pmatrix} \tag{A.63}$$

the vector-valued function $\widehat{\mathbf{f}}$ can be represented according to

$$\widehat{\mathbf{f}}(k_r,k_\vartheta,k_\phi) = f_{k_r}\mathbf{e}_{k_r} + f_{k_\vartheta}\mathbf{e}_{k_\vartheta} + f_{k_\phi}\mathbf{e}_{k_\phi} \tag{A.64}$$

Due to spherical symmetry $\widehat{\mathbf{f}}$ is only a function of the radius $k_r = |\mathbf{k}|$. Therefore, all other contributions besides the radial one equal zero, leading to

$$\widehat{\mathbf{f}}(k_r, k_\vartheta, k_\phi) = f_{k_r}\begin{pmatrix}\cos k_\phi \sin k_\vartheta \\ \sin k_\phi \sin k_\vartheta \\ \cos k_\vartheta\end{pmatrix} \tag{A.65}$$

Applying the inverse Fourier transform yields

$$\begin{aligned}\mathbf{f}(r) \quad = \quad & \int_{k_r=0}^{\infty}\int_{k_\vartheta=0}^{\pi}\int_{k_\varphi=0}^{2\pi}\begin{pmatrix}\widehat{f}_{k_r}(k_r)\cos k_\varphi \sin k_\vartheta \\ \widehat{f}_{k_r}(k_r)\sin k_\varphi \sin k_\vartheta \\ \widehat{f}_{k_r}(k_r)\cos k_\vartheta\end{pmatrix} \\ & \times \mathrm{e}^{2\pi \mathrm{i}\, rk_r \cos k_\vartheta} k_r^2 \sin k_\vartheta \,\mathrm{d}k_\varphi \,\mathrm{d}k_\vartheta \,\mathrm{d}k_r\end{aligned} \tag{A.66}$$

Performing the integration over k_ϕ leads to vanishing contributions for the first and second vector entry due to $\int_{k_\phi=0}^{2\pi}\cos k_\phi \,\mathrm{d}k_\phi = 0$ and $\int_{k_\phi=0}^{2\pi}\sin k_\phi \,\mathrm{d}k_\phi = 0$. As a result, we only regard the z-direction, leading to

$$\mathbf{f}(r) = \int_{k_r=0}^{\infty}\int_{k_\vartheta=0}^{\pi}\widehat{f}_{k_r}(k_r)\begin{pmatrix}0\\0\\2\pi\cos k_\vartheta\end{pmatrix}\mathrm{e}^{2\pi \mathrm{i}\, rk_r \cos k_\vartheta} k_r^2 \sin k_\vartheta \,\mathrm{d}k_\vartheta \,\mathrm{d}k_r \tag{A.67}$$

With $(0,0,2\pi\cos k_\vartheta)^\top = 2\pi\cos k_\vartheta \mathbf{e}_{k_z}$, eq. (A.67) yields

$$\mathbf{f}(r) = \mathbf{e}_{k_z}\int_{k_r=0}^{\infty}\int_{k_\vartheta=0}^{\pi}\widehat{f}_{k_r}(k_r) 2\pi \cos k_\vartheta \mathrm{e}^{2\pi \mathrm{i}\, rk_r \cos k_\vartheta} k_r^2 \sin k_\vartheta \,\mathrm{d}k_\vartheta \,\mathrm{d}k_r \tag{A.68}$$

Integration over k_ϑ is carried out using the substitution $u = \cos k_\vartheta$ and $\mathrm{d}u = -\sin k_\vartheta \,\mathrm{d}\vartheta$ followed by partial integration, leading to

$$\begin{aligned}\mathbf{f}(r) &= -\mathbf{e}_{k_z}\int_{k_r=0}^{\infty}\int_{u=1}^{-1}\widehat{f}_{k_r}(k_r) 2\pi u \mathrm{e}^{2\pi \mathrm{i}\, rk_r u} k_r^2 \,\mathrm{d}u \,\mathrm{d}k_r \\ &= \mathbf{e}_{k_z}\int_{k_r=0}^{\infty}\widehat{f}_{k_r}(k_r)\left(\frac{\mathrm{e}^{-2\pi \mathrm{i}\, rk_r} + \mathrm{e}^{2\pi \mathrm{i}\, rk_r}}{\mathrm{i}\, rk_r} + \frac{\mathrm{e}^{-2\pi \mathrm{i}\, rk_r} - \mathrm{e}^{2\pi \mathrm{i}\, rk_r}}{2\pi(\mathrm{i}\, rk_r)^2}\right)k_r^2 \,\mathrm{d}k_r\end{aligned} \tag{A.69}$$

Using Euler's formula yields

$$\begin{aligned}\mathbf{f}(r) \quad = \quad & \mathbf{e}_{k_z}\frac{\mathrm{i}}{\pi r^2}\int_{k_r=0}^{\infty}\widehat{f}_{k_r}(k_r)\sin(2\pi rk_r)\,\mathrm{d}k_r \\ & -\mathbf{e}_{k_z}\frac{2\mathrm{i}}{r}\int_{k_r=0}^{\infty}\widehat{f}_{k_r}(k_r)k_r\cos(2\pi rk_r)\,\mathrm{d}k_r\end{aligned} \tag{A.70}$$

Due to alignment of the vector $\mathbf{r}$ in Fourier space with $\mathbf{e}_{k_z}$, implying $\mathbf{e}_r = \mathbf{e}_{k_z}$ we obtain a combination of sine and cosine transform, according to

$$\mathbf{f}(r) = \mathbf{e}_r\frac{\mathrm{i}}{\pi r^2}\mathscr{SIN}\left[\widehat{f}_{k_r}(k_r)\right] - \mathbf{e}_r\frac{2\mathrm{i}}{r}\mathscr{COS}\left[\widehat{f}_{k_r}(k_r)k_r\right] \tag{A.71}$$

Note that the forward Fourier transform, eq. (A.62), differs slightly from the inverse transform, eq. (A.71).

Appendix B. Computation of First Order Hankel Transform with Algorithm for Zeroth Order

In the following, we derive a way to compute the Hankel transform of first order with algorithms solving the Hankel transform of zeroth order. The Hankel transform of first order is defined as

$$\mathscr{H}_1[f(r)] = 2\pi\int_{r=0}^{\infty} f(r)\mathrm{J}_1(2\pi rk_r)r\,\mathrm{d}r \tag{B.1}$$

with the Bessel function of first kind and first order J_1. Exploiting $\mathrm{J}_1(r) = -\mathrm{J}_0'(r)$, with the derivative with respect to r of the Bessel function of first kind and zeroth order J_0', and the coordinate transform $r = \frac{x}{2\pi k_r} \rightarrow \mathrm{d}r = \frac{\mathrm{d}x}{2\pi k_r}$, leads to

$$\mathscr{H}_1[f(r)] = -\frac{1}{2\pi k_r^2}\int_{x=0}^{\infty} f\left(\frac{x}{2\pi k_r}\right)\mathrm{J}_0{}'(x)x\,\mathrm{d}x \tag{B.2}$$

Integration by parts with vanishing integration bounds $\left[f\left(\frac{x}{2\pi k_r}\right)\mathrm{J}_0(x)x\right]_0^\infty = 0$ leaves us with

$$\begin{aligned}\mathscr{H}_1[f(r)] \quad &= \quad \frac{1}{2\pi k_r^2}\int_{x=0}^{\infty}\left(\frac{x}{2\pi k_r}f'\left(\frac{x}{2\pi k_r}\right) + f\left(\frac{x}{2\pi k_r}\right)\right)\mathrm{J}_0(x)\,\mathrm{d}x \\ &= \quad \frac{1}{k_r}\int_{r=0}^{\infty}\left(\frac{f(r)}{r} + f'(r)\right)\mathrm{J}_0(2\pi rk_r)r\,\mathrm{d}r \\ &= \quad \frac{1}{2\pi k_r}\mathscr{H}_0\left[\frac{f(r)}{r} + f'(r)\right]\end{aligned} \tag{B.3}$$

where the prime $(')$ denotes the derivative with respect to r. Instead of computing the discrete Hankel transform on a logarithmic grid as was done by Boţan et al. [18] or Hamilton [60], we follow the approach of Hansen [52–54] and compute the Hankel transform on an equidistant grid by a combination of the fast Abel and fast Fourier transform. The algorithm used for the fast Abel transform is described below.

Appsendix C. Computation of the Abel and inverse Abel Transform

The algorithm for the Abel transform is taken from Hansen [53] and Hansen and Law [54]. The recursive scheme computes the Abel and inverse Abel transform on an equidistant grid with N grid points, using the parameters given in Table C.1. We define the grid in radial direction as depicted in Fig. 2.

The algorithm described in eq. (C.1) computes the forward and inverse Abel transform using a low order state-space model (dimension $K = 9$). The input of the linear system is the first-order hold approximation of the discrete function f_n to be transformed, leading to

$$\mathbf{x}_{n-1} = \Phi_n\mathbf{x}_n + B_{0,n}f_n + B_{1,n}f_{n-1} \tag{C.1a}$$

$$F_n = C\mathbf{x}_n \tag{C.1b}$$

$$\mathbf{x}_N = 0 \tag{C.1c}$$

$$\Phi_n = \mathrm{diag}\left\{ \left(\frac{r_n}{r_{n-1}}\right)^{\lambda_1}, \cdots, \left(\frac{r_n}{r_{n-1}}\right)^{\lambda_K} \right\} \tag{C.1d}$$

$$\mathrm{C} = [1, \cdots, 1] \tag{C.1e}$$

$$B_{0,n} = \left[h_1 \beta_{0,n}(\lambda_1), \cdots, h_K \beta_{0,n}(\lambda_K)\right]^\top \tag{C.1f}$$

$$B_{1,n} = \left[h_1 \beta_{1,n}(\lambda_1), \cdots, h_K \beta_{1,n}(\lambda_K)\right]^\top \tag{C.1g}$$

with the grid point index n, the grid dependent states of the state-space model $\mathbf{x}_n$, the grid dependent state transition matrix Φ_n, the grid dependent input vectors $B_{0,n}$ and $B_{1,n}$, the discrete (inverse) Abel transform F_n, the output vector of the state-space representation of the linear system C, the radial grid points r_n, as well as the model parameters from Hansen [52,54], λ_k and h_k (see Table C.1). The recursion is started at the outermost grid point r_N with $\mathbf{x}_N = 0$ and is continued inwards toward the center of the radial grid. This method cannot be used if $r_{n-1} = 0$. For the forward transform one uses $\beta^{\mathrm{f}}_{0,n}$ and $\beta^{\mathrm{f}}_{1,n}$, obtained from

$$\beta^{\mathrm{f}}_{0,n}(\lambda_k) = \frac{2r_{n-1}}{r_n - r_{n-1}} \frac{r_{n-1} + [r_n(\lambda_k+1) - r_{n-1}(\lambda_k+2)]\left(\frac{r_n}{r_{n-1}}\right)^{\lambda_k+1}}{(\lambda_k+1)(\lambda_k+2)} \tag{C.2a}$$

$$\beta^{\mathrm{f}}_{1,n}(\lambda_k) = \frac{2r_{n-1}}{r_n - r_{n-1}} \frac{[r_{n-1}(\lambda_k+1) - r_n(\lambda_k+2)] + r_n\left(\frac{r_n}{r_{n-1}}\right)^{\lambda_k+1}}{(\lambda_k+1)(\lambda_k+2)} \tag{C.2b}$$

For the inverse transform one uses $\beta^{\mathrm{b}}_{0,n}$ and $\beta^{\mathrm{b}}_{1,n}$, according to

$$\beta^{\mathrm{b}}_{0,n}(\lambda_k) = \begin{cases} -\dfrac{1}{\pi(r_n - r_{n-1})} \ln\left(\dfrac{r_n}{r_{n-1}}\right) & \lambda_k = 0 \\ \dfrac{1}{\pi\lambda_k(r_n - r_{n-1})}\left(1 - \left(\dfrac{r_n}{r_{n-1}}\right)^{\lambda_k}\right) & \lambda_k \neq 0 \end{cases} \tag{C.3a}$$

$$\beta^{\mathrm{b}}_{1,n}(\lambda_k) = -\beta^{\mathrm{b}}_{0,n}(\lambda_k) \tag{C.3b}$$

Table C.1
Parameters for Abel transform [52].

k	h_k/π	λ_k
1	0.318	0
2	0.19	−2.1
3	0.35	−6.2
4	0.82	−22.4
5	1.8	−92.5
6	3.9	−414.5
7	8.3	−1889.4
8	19.6	−8990.9
9	48.3	−47391.1

Appendix D. Discrete Sine- & Cosine Transforms

In this work in sections 4.2.2 and 4.3.2 we used the discrete versions of the sine and cosine transforms. Both transforms transform between a finite series of equally-spaced samples $j = 0, \cdots, (N-1)$ of a function f_j in real space, and a series of equal length and equally-spaced samples $k = 0, \cdots, (N-1)$ in Fourier space $\widehat{f}_k$. The index j denotes the discrete grid points in real space, while k denotes the grid points in Fourier space.

The discrete sine transforms $\mathscr{DST}_{\mathrm{II}}$ and $\mathscr{DST}_{\mathrm{III}}$ of the function f are defined by

$$\widehat{f}_{k^*}^{\mathscr{DST}_{\mathrm{II}}} = \sum_{j=0}^{N-1} f_j \sin\left[\frac{\pi}{N}\left(j+\frac{1}{2}\right)(k^*+1)\right] \quad \text{with } k^* = 0, \cdots, (N-1) \tag{D.1a}$$

$$f_j^{\mathscr{DST}_{\mathrm{III}}} = \frac{(-1)^j}{2}\widehat{f}_{N-1} + \sum_{k^*=0}^{N-2} \widehat{f}_{k^*} \sin\left[\frac{\pi}{N}(k^*+1)\left(j+\frac{1}{2}\right)\right] \quad \text{with } j = 0, \cdots, (N-1) \tag{D.1b}$$

with the number of discrete grid points N, where the iteration variable k^* does not represent the true Fourier variable k, which for the discrete sine transforms is obtained from $k = k^* + 1$.

The $\mathscr{DST}_{\mathrm{II}}$ assumes the function f_j to be odd around $j = \left(-\frac{1}{2}\right)$ and $j = \left(N - \frac{1}{2}\right)$ (equivalent to $r = 0$ and $r = L_{\mathrm{tot}}$ in Fig. 3). However, the $\mathscr{DST}_{\mathrm{III}}$ implies the function $\widehat{f}_{k^*}$ to be odd around $k^* = (-1)$ and even around $k^* = (N-1)$ (equivalent to $k = 0$ and $k = N$, respectively). Both discrete sine transforms are scaled with the factor $\eta = \frac{1}{\sqrt{2N}}$ allowing usage of the two transforms as direct inverses of each other: $\mathscr{DST}_{\mathrm{II}}^{-1} = \mathscr{DST}_{\mathrm{III}}$.

The discrete cosine transforms $\mathscr{DCT}_{\mathrm{II}}$ and $\mathscr{DCT}_{\mathrm{III}}$ are defined by

$$\widehat{f}_k^{\mathscr{DCT}_{\mathrm{II}}} = \sum_{j=0}^{N-1} f_j \cos\left[\frac{\pi}{N}\left(j+\frac{1}{2}\right)k\right] \quad \text{with } k = 0, \cdots, (N-1) \tag{D.2a}$$

$$f_j^{\mathscr{DCT}_{\mathrm{III}}} = \frac{1}{2}\widehat{f}_0 + \sum_{k=1}^{N-1} \widehat{f}_k \cos\left[\frac{\pi}{N}k\left(j+\frac{1}{2}\right)\right] \quad \text{with } j = 0, \cdots, (N-1) \tag{D.2b}$$

The $\mathscr{DCT}_{\mathrm{II}}$ assumes the function f_j to be even around $j = \left(-\frac{1}{2}\right)$ and $j = \left(N - \frac{1}{2}\right)$ (equivalent to $r = 0$ and $r = L_{\mathrm{tot}}$ in Fig. 3). However, the $\mathscr{DCT}_{\mathrm{III}}$ implies the function $\widehat{f}_k$ to be even around $k = 0$ and odd around $k = N$. Both discrete cosine transforms are scaled with the factor $\eta = \frac{1}{\sqrt{2N}}$ allowing usage of the two transforms as direct inverses of each other: $\mathscr{DCT}_{\mathrm{II}}^{-1} = \mathscr{DCT}_{\mathrm{III}}$.

Appendix E. Reducing Gibbs Phenomenon via the Lanczos σ-factor

Fourier transform algorithms applied to very sharp density profiles or non-periodic boundary conditions, as used for Cartesian coordinates in section 4.1.1, can cause ringing artifacts at profile discontinuities (Gibbs phenomenon). These artifacts can be reduced by multiplication of the Fourier space representation of the function with the Lanczos σ-factor [61].

$$\sigma(k) = \mathrm{sinc}\frac{k}{M} = \frac{\sin\pi\frac{k}{M}}{\pi\frac{k}{M}} \tag{E.1}$$

with the Fourier variable k, and where M denotes the number of k-values in the dimension of interest ($k = 0, \cdots, M-1$). For the FFT with an even number of grid points we get $M = \frac{N}{2} + 1$, with N as the number of grid points (see eqs. (54) and (55)). For fast sine & cosine transforms $M = (N+1)$ and $M = N$ hold, respectively (see eqs. (75) and (76)).

The procedure can easily be implemented by multiplying the weight functions with the σ-factor. For multidimensional Fourier transforms, the σ-factor has to be multiplied for every dimension separately. For example, for 3-D Cartesian, 2-D cylindrical and 1-D spherical coordinates the Lanczos σ-factor is computed as

$$\widehat{\omega}_i^{\sigma}(\mathbf{k}) = \widehat{\omega}_i(k_x, k_y, k_z)\sigma_x(k_x)\sigma_y(k_y)\sigma_z(k_z) \tag{E.2a}$$

$$\widehat{\omega}_i^{\sigma}(\mathbf{k}) = \widehat{\omega}_i(k_z, k_r)\sigma_z(k_z)\sigma_r(k_r) \tag{E.2b}$$

$$\widehat{\omega}_i^{\sigma}(\mathbf{k}) = \widehat{\omega}_i(k_r)\sigma_r(k_r) \tag{E.2c}$$

For increased smoothing, the weight function can be multiplied with the σ-factor multiple times.

For Cartesian coordinates, robustness of the FFT can further be increased by enforcing periodic boundary conditions via an additional domain, with respect to the ones displayed in Fig. 1, using a smooth transition function (for example the hyperbolic tangent). The sine and cosine transform inherently possess this property. Enforcing periodic boundary conditions is only relevant if no Lanczos σ-factor is used.

Appendix F. Comparison of Convolution Results in different Coordinate Systems

Computation of the convolution integrals discussed in section 3 depends on the underlying coordinate system. Fig. F.7 presents results of three convolutions of density profile ρ with different weight functions from FMT [57], obtaining weighted densities n_0, n_3 and n_{V1}, for Cartesian, cylindrical and spherical coordinates. The remaining weighted densities (n_1, n_2 and n_{V1}) differ from the considered ones only by a constant, and are thus not shown here.

For $r \to \infty$ the convolution results are not dependent on the underlying coordinate system. Only for small systems, such as the system depicted here, deviations occur. The weighted densities in the region from 0 Å to 1 Å and 2 Å to 3 Å are equivalent for the three coordinate systems, while differences are revealed between 1 Å to 2 Å in the influence length $R = 0.5$ Å of the weight function around the density jump at $r = 1.5$ Å. Between 1 Å and 2 Å, the scalar-valued weighted densities are smaller for cylindrical, and smallest for spherical coordinates, compared to Cartesian coordinates. The maximum of the vector-valued weighted densities lies directly on the density step for Cartesian coordinates, while for cylindrical and spherical coordinate systems the maximum is shifted towards smaller radii.

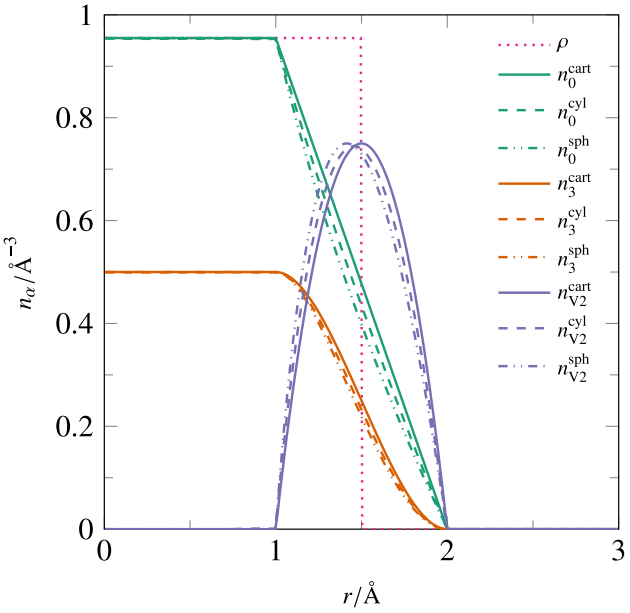

Fig. F.7. Comparison of one-dimensional convolutions in Cartesian, cylindrical and spherical coordinates presenting weighted densities n_0, n_3 and n_{V2} for a hard-sphere fluid with radius $R = 0.5$ Å modeled with FMT [57]. The density profile is given as a Heaviside step function $\rho(r) = \frac{3}{\pi}\Theta(1.5\text{Å} - r)\,\text{Å}^{-3}$.

Appendix G. Supplementary data

Supplementary data to this article can be found online at https://doi.org/10.1016/j.fluid.2019.112306.

References

[1] M.G. Knepley, D.A. Karpeev, S. Davidovits, R.S. Eisenberg, D. Gillespie, An efficient algorithm for classical density functional theory in three dimensions: ionic solutions, J. Chem. Phys. 132 (12) (2010) 124101. https://doi.org/10.1063/1.3357981.

[2] Y. Rosenfeld, Free-energy model for the inhomogeneous hard-sphere fluid mixture and density-functional theory of freezing, Phys. Rev. Lett. 63 (1989) 980–983. https://doi.org/10.1103/PhysRevLett.63.980.

[3] L.J.D. Frink, A.G. Salinger, M.P. Sears, J.D. Weinhold, A.L. Frischknecht, Numerical challenges in the application of density functional theory to biology and nanotechnology, J. Phys. Condens. Matter 14 (46) (2002) 12167. https://doi.org/10.1088/0953-8984/14/46/320.

[4] L.J.D. Frink, M.G. Martin, A.G. Salinger, M.A. Heroux, High performance computing for the application of molecular theories to biological systems, J. Phys. Conf. Ser. 46 (1) (2006) 304. https://doi.org/10.1088/1742-6596/46/1/042.

[5] M.P. Sears, L.J. Frink, A new efficient method for density functional theory calculations of inhomogeneous fluids, J. Comput. Phys. 190 (1) (2003) 184–200. https://doi.org/10.1016/S0021-9991(03)00270-5.

[6] S.P. Hlushak, W. Rżysko, S. Sokołowski, Density functional study of flexible chain molecules at curved surfaces, J. Chem. Phys. 131 (9) (2009), 094904. https://doi.org/10.1063/1.3213623.

[7] S.P. Hlushak, C. McCabe, P.T. Cummings, Fourier space approach to the classical density functional theory for multi-Yukawa and square-well fluids, J. Chem. Phys. 137 (10) (2012) 104104. https://doi.org/10.1063/1.4749381.

[8] S.P. Hlushak, P.T. Cummings, C. McCabe, Comparison of several classical density functional theories for the adsorption of flexible chain molecules into cylindrical nanopores, J. Chem. Phys. 139 (23) (2013) 234902. https://doi.org/10.1063/1.4843655.

[9] M. Oettel, S. Görig, A. Härtel, H. Löwen, M. Radu, T. Schilling, Free energies, vacancy concentrations, and density distribution anisotropies in hard-sphere crystals: a combined density functional and simulation study, Phys. Rev. E 82 (2010), 051404. https://doi.org/10.1103/PhysRevE.82.051404.

[10] M. Oettel, S. Dorosz, M. Berghoff, B. Nestler, T. Schilling, Description of hard-sphere crystals and crystal-fluid interfaces: a comparison between density functional approaches and a phase-field crystal model, Phys. Rev. E 86 (2012),

021404. https://doi.org/10.1103/PhysRevE.86.021404.
[11] X. Wang, J. Mi, C. Zhong, Density functional theory for crystal-liquid interfaces of Lennard-Jones fluid, J. Chem. Phys. 138 (16) (2013) 164704. https://doi.org/10.1063/1.4802633.
[12] M. Levesque, R. Vuilleumier, D. Borgis, Scalar fundamental measure theory for hard spheres in three dimensions: application to hydrophobic solvation, J. Chem. Phys. 137 (3) (2012) 34115. https://doi.org/10.1063/1.4734009.
[13] Y. Liu, S. Zhao, J. Wu, A site density functional theory for water: application to solvation of amino acid side chains, J. Chem. Theory Comput. 9 (4) (2013) 1896–1908. https://doi.org/10.1021/ct3010936.
[14] D. Zhou, J. Mi, C. Zhong, Three-dimensional density functional study of heterogeneous nucleation of droplets on solid surfaces, J. Phys. Chem. B 116 (48) (2012) 14100–14106. https://doi.org/10.1021/jp307820w.
[15] A. González, J.A. White, F.L. Román, S. Velasco, Density functional theory of fluids in nanopores: analysis of the fundamental measures theory in extreme dimensional-crossover situations, J. Chem. Phys. 125 (6) (2006), 064703. https://doi.org/10.1063/1.2227389.
[16] A. Malijevský, Fundamental measure theory in cylindrical geometry, J. Chem. Phys. 126 (13) (2007) 134710. https://doi.org/10.1063/1.2713106.
[17] N.J. Mariani, C. Mocciaro, M.A. Campesi, G.F. Barreto, On the computation of fundamental measure theory in pores with cylindrical symmetry, J. Chem. Phys. 132 (20) (2010) 204104. https://doi.org/10.1063/1.3425873.
[18] V. Boţan, F. Pesth, T. Schilling, M. Oettel, Hard-sphere fluids in annular wedges: density distributions and depletion potentials, Phys. Rev. E 79 (2009), 061402. https://doi.org/10.1103/PhysRevE.79.061402.
[19] R. Roth, Fundamental measure theory for hard-sphere mixtures: a review, J. Phys. Condens. Matter 22 (6) (2010), 063102, https://doi.org/10.1088/0953-8984/22/6/063102.
[20] P. Yatsyshin, N. Savva, S. Kalliadasis, Spectral methods for the equations of classical density-functional theory: relaxation dynamics of microscopic films, J. Chem. Phys. 136 (12) (2012) 124113. https://doi.org/10.1063/1.3697471.
[21] P. Yatsyshin, N. Savva, S. Kalliadasis, Wetting of prototypical one- and two-dimensional systems: thermodynamics and density functional theory, J. Chem. Phys. 142 (3) (2015) 34708. https://doi.org/10.1063/1.4905605.
[22] A. Nold, B.D. Goddard, P. Yatsyshin, N. Savva, S. Kalliadasis, Pseudospectral methods for density functional theory in bounded and unbounded domains, J. Comput. Phys. 334 (2017) 639–664. https://doi.org/10.1016/j.jcp.2016.12.023.
[23] X. Xu, D. Cao, Multiscaled density-functional theory for helical polymers, J. Chem. Phys. 131 (5) (2009) 54901, https://doi.org/10.1063/1.3197004.
[24] A. Kovalenko, S. Ten-no, F. Hirata, Solution of three-dimensional reference interaction site model and hypernetted chain equations for simple point charge water by modified method of direct inversion in iterative subspace, J. Comput. Chem. 20 (9) (1999) 928–936, https://doi.org/10.1002/(SICI)1096-987X(19990715)20:9<928::AID-JCC4>3.0.CO;2-X2-X.
[25] L.J.D. Frink, A.G. Salinger, Two- and three-dimensional nonlocal density functional theory for inhomogeneous fluids, J. Comput. Phys. 159 (2) (2000) 407–424. https://doi.org/10.1006/jcph.2000.6454.
[26] L.J.D. Frink, A.G. Salinger, Two- and three-dimensional nonlocal density functional theory for inhomogeneous fluids, J. Comput. Phys. 159 (2) (2000) 425–439. https://doi.org/10.1006/jcph.2000.6455.
[27] L.J.D. Frink, A.L. Frischknecht, M.A. Heroux, M.L. Parks, A.G. Salinger, Toward quantitative coarse-grained models of lipids with fluids density functional theory, J. Chem. Theory Comput. 8 (4) (2012) 1393–1408. https://doi.org/10.1021/ct200707b.
[28] J. Mairhofer, J. Gross, Numerical aspects of classical density functional theory for one-dimensional vapor-liquid interfaces, Fluid Phase Equilib. 444 (1 − 12) (2017). https://doi.org/10.1016/j.fluid.2017.03.023.
[29] J. Gross, G. Sadowski, Application of perturbation theory to a hard-chain reference fluid: an equation of state for square-well chains, Fluid Phase Equilib. 168 (2) (2000) 183–199. https://doi.org/10.1016/S0378-3812(00)00302-2.
[30] J. Gross, G. Sadowski, Perturbed-chain SAFT: an equation of state based on a perturbation theory for chain molecules, Ind. Eng. Chem. Res. 40 (4) (2001) 1244–1260. https://doi.org/10.1021/ie0003887.
[31] J. Gross, G. Sadowski, Modeling polymer systems using the perturbed-chain statistical associating fluid theory equation of state, Ind. Eng. Chem. Res. 41 (5) (2002) 1084–1093. https://doi.org/10.1021/ie010449g.
[32] J. Gross, G. Sadowski, Application of the perturbed-chain SAFT equation of state to associating systems, Ind. Eng. Chem. Res. 41 (22) (2002) 5510–5515. https://doi.org/10.1021/ie010954d.
[33] M.S. Wertheim, Fluids with highly directional attractive forces. I. Statistical thermodynamics, J. Stat. Phys. 35 (1) (1984) 19–34. https://doi.org/10.1007/BF01017362.
[34] M.S. Wertheim, Fluids with highly directional attractive forces. II. Thermodynamic perturbation theory and integral equations, J. Stat. Phys. 35 (1) (1984) 35–47. https://doi.org/10.1007/BF01017363.
[35] M.S. Wertheim, Fluids with highly directional attractive forces. III. Multiple attraction sites, J. Stat. Phys. 42 (3) (1986) 459–476. https://doi.org/10.1007/BF01127721.
[36] M.S. Wertheim, Fluids with highly directional attractive forces. IV. Equilibrium polymerization, J. Stat. Phys. 42 (3) (1986) 477–492. https://doi.org/10.1007/BF01127722.
[37] W.G. Chapman, G. Jackson, K.E. Gubbins, Phase equilibria of associating fluids, Mol. Phys. 65 (5) (1988) 1057–1079. https://doi.org/10.1080/00268978800101601.
[38] J. Gross, An equation-of-state contribution for polar components: quadrupolar molecules, AIChE J. 51 (9) (2005) 2556–2568. https://onlinelibrary.wiley.com/doi/abs/10.1002/aic.10502.
[39] J. Gross, J. Vrabec, An equation-of-state contribution for polar components: dipolar molecules, AIChE J. 52 (3) (2006) 1194–1204. https://onlinelibrary.wiley.com/doi/abs/10.1002/aic.10683.
[40] J. Vrabec, J. Gross, Vapor–liquid equilibria simulation and an equation of state contribution for dipole–quadrupole interactions, J. Phys. Chem. B 112 (1) (2008) 51–60. https://doi.org/10.1021/jp072619u.
[41] J. Gross, A density functional theory for vapor–liquid interfaces using the PCP-SAFT equation of state, J. Chem. Phys. 131 (20) (2009) 204705. https://doi.org/10.1063/1.3263124.
[42] C. Klink, J. Gross, A density functional theory for vapor–liquid interfaces of mixtures using the perturbed-chain polar statistical associating fluid theory equation of state, Ind. Eng. Chem. Res. 53 (14) (2014) 6169–6178. https://doi.org/10.1021/ie4029895.
[43] C. Klink, B. Planková, J. Gross, Density functional theory for liquid–liquid interfaces of mixtures using the perturbed-chain polar statistical associating fluid theory equation of state, Ind. Eng. Chem. Res. 54 (16) (2015) 4633–4642. https://doi.org/10.1021/acs.iecr.5b00445.
[44] C. Klink, C. Waibel, J. Gross, Analysis of interfacial transport resistivities of pure components and mixtures based on density functional theory, Ind. Eng. Chem. Res. 54 (45) (2015) 11483–11492. https://doi.org/10.1021/acs.iecr.5b03270.
[45] G. Lamanna, C. Steinhausen, B. Weigand, A. Preusche, B. Bork, A. Dreizler, R. Stierle, J. Gross, On the importance of non-equilibrium models for describing the coupling of heat and mass transfer at high pressure, Int. Commun. Heat Mass Transf. 98 (49–58) (2018). https://doi.org/10.1016/j.icheatmasstransfer.2018.07.012.
[46] E. Sauer, J. Gross, Classical density functional theory for liquid–fluid interfaces and confined systems: a functional for the perturbed-chain polar statistical associating fluid theory equation of state, Ind. Eng. Chem. Res. 56 (14) (2017) 4119–4135. https://doi.org/10.1021/acs.iecr.6b04551.
[47] E. Sauer, A. Terzis, M. Theiss, B. Weigand, J. Gross, Prediction of contact angles and density profiles of sessile droplets using classical density functional theory based on the PCP-SAFT equation of state, Langmuir 34 (42) (2018) 12519–12531, https://doi.org/10.1021/acs.langmuir.8b01985.
[48] G. Shen, X. Ji, X. Lu, A hybrid perturbed-chain SAFT density functional theory for representing fluid behavior in nanopores, J. Chem. Phys. 138 (22) (2013) 224706. https://doi.org/10.1063/1.4808160.
[49] G. Shen, X. Ji, S. Öberg, X. Lu, A hybrid perturbed-chain SAFT density functional theory for representing fluid behavior in nanopores: Mixtures, J. Chem. Phys. 139 (19) (2013) 194705. https://doi.org/10.1063/1.4825078.
[50] Z. Ye, J. Cai, H. Liu, Y. Hu, Density and chain conformation profiles of square-well chains confined in a slit by density-functional theory, J. Chem. Phys. 123 (19) (2005) 194902. https://doi.org/10.1063/1.2117009.
[51] X. Xu, D.E. Cristancho, S. Costeux, Z.-G. Wang, Density-functional theory for polymer-carbon dioxide mixtures: a perturbed-chain SAFT approach, J. Chem. Phys. 137 (5) (2012), 054902. https://doi.org/10.1063/1.4742346.
[52] E.W. Hansen, Fast Hankel transform algorithm, IEEE Trans. Acoust. Speech Signal Process. 33 (3) (1985) 666–671, https://doi.org/10.1109/TASSP.1985.1164579.
[53] E.W. Hansen, Correction to "fast Hankel transform algorithm", IEEE Trans. Acoust. Speech Signal Process. 34 (3) (1986) 623–624, https://doi.org/10.1109/TASSP.1986.1164860.
[54] E.W. Hansen, P.-L. Law, Recursive methods for computing the Abel transform and its inverse, J. Opt. Soc. Am. A 2 (4) (1985) 510–520, https://doi.org/10.1364/JOSAA.2.000510.
[55] P.N. Swarztrauber, Parallel Computations, Academic Press, New York, 1982, https://doi.org/10.1016/B978-0-12-592101-5.50007-5.
[56] P.N. Swarztrauber, FFT algorithms for vector computers, Parallel Comput. 1 (1) (1984) 45–63. https://doi.org/10.1016/S0167-8191(84)90413-7.
[57] R. Roth, R. Evans, A. Lang, G. Kahl, Fundamental measure theory for hard-sphere mixtures revisited: the White Bear version, J. Phys. Condens. Matter 14 (46) (2002) 12063, https://doi.org/10.1088/0953-8984/14/46/313.
[58] Y.-X. Yu, J. Wu, Structures of hard-sphere fluids from a modified fundamental-measure theory, J. Chem. Phys. 117 (22) (2002) 10156–10164, https://doi.org/10.1063/1.1520530.
[59] T. Butz, Fourier Transformation for Pedestrians, Springer, 2006, https://doi.org/10.1007/978-3-319-16985-9.
[60] A.J.S. Hamilton, Uncorrelated modes of the non-linear power spectrum, Mon. Not. R. Astron. Soc. 312 (2) (2000) 257–284, https://doi.org/10.1046/j.1365-8711.2000.03071.x.
[61] C. Lanczos, Applied Analysis, Prentice-Hall Mathematics Series, Prentice-Hall, 1956.